III. R & D RELATED TO A FUTURE RARE ISOTOPE ACCELERATOR FACILITY

OVERVIEW

The Rare Isotope Accelerator (RIA), a next-generation facility for basic research in nuclear physics, is a high priority for construction in the United States by the Department of Energy. The overall concept for RIA was developed during 1999 by the ISOL Task Force, a sub-committee of the Nuclear Science Advisory Committee (NSAC). A preliminary cost analysis of the RIA project was developed jointly by Argonne National Laboratory and the National Superconducting Cyclotron Laboratory of Michigan State University. The costs were reviewed by another sub-committee of NSAC in January 2001. It is possible the Conceptual Design of RIA could begin in 2004 following the DOE Critical Decision 0 which is the Mission Need Statement for RIA. In the meantime, to prepare for construction on this time scale it is essential to continue a vigorous R&D program for RIA. This section is a progress report on the RIA R&D efforts at Argonne.

The RIA R&D topics addressed at Argonne during the year 2002 fall under four main categories: RIA Beam Dynamics, Superconducting Linac Technology, and Rare Isotope Production, Separation and Diagnostics, sections A-C below.

We continued to develop and improve the baseline design for the RIA proposal. Highlights of developments during 2002 include:

- Extensive refinements of the beam dynamics simulations and improvements to the lattice of the RIA Driver Linac including the development of an alternative baseline design using triple-spoke resonators in place of the reduced-beta elliptical resonators.
- Completion of the design and initiation of the construction of the three types of SC drift-tube resonators required for the mid-velocity regime of the RIA Driver Linac.
- Completion of a preliminary engineering design for a 57.5-MHz CW room-temperature RFQ for the front end of the RIA Driver Linac.
- Construction of a half-scale cold model of the proposed hybrid RFQ for the RIA Post Accelerator.
- Completion and initial testing of the prototype windowless liquid lithium fragmentation target.
- Development of a general 3-D Monte Carlo model for the simulation of the effusion process for radioactive isotopes from complex ISOL target/ion source configurations.

A. RIA BEAM DYNAMICS

a.1. Beam Dynamics Studies Related To The RIA Project (P. N. Ostroumov, V. N. Aseev, K. W. Shepard)

Beam dynamics studies were focused on the development of an end-to-end simulation code both for driver linac and post-accelerator. In addition, the overall linac design has been continuously improved by optimization of the accelerator systems.

Development of simulation code TRACK

It is important to have beam dynamics simulation code both for the cost-effective design of the RIA linacs and detailed calculations of beam parameters in the facility. The TRACK code was substantially modified during past year. Presently the code is capable of end-to-end simulations both for the driver linac and post-accelerator. The code has the following features:

- Multiparticle simulation of multiple component ion beams in six-dimensional phase space;
- 3D electromagnetic fields in rectangular mesh from the electromagnetic code Microwave Studio can be inserted into the TRACK;
- Integration of equations of motion by 4th order Runge-Kutta method;
- Fringing fields of magnets and multipoles are defined using the method of Enge coefficients;
- Realistic field distribution in solenoids;
- Misalignments of focusing elements and random errors of the electromagnetic fields are included;

- Space charge of multiple component ion beams is included;
- Regeneration of the particle distribution after the passage through stripping foils and films on the base of the SRIM code;

Currently TRACK can calculate charged-particle trajectories through the following elements:

- Any type of accelerating resonator with realistic 3D fields;
- Bending magnets with fringing fields;
- Multipoles (quadrupoles, sextupoles, …) with fringing fields;
- Solenoids with realistic field distribtions;
- RFQs;
- Multi-harmonic bunchers;
- Axial-symmetric electrostatic lenses;
- Change of electric potential (entrance/exit of a HV deck);
- Beam steering elements;
- Beam collimators;
- Stripper foils.

Front End of the driver linac

Detailed simulation of two-charge-state heavy ion beams in the Front End of the driver linac was performed. Beam distribution after the RFQ was obtained by simulation of a large number of particles ($\sim 10^5$) through the LEBT and RFQ. A strong coupling of the longitudinal and transverse motions in the beginning of the RFQ takes place. Due to the low velocity of particles in the heavy-ion RFQs the Hamiltonian of longitudinal motion depends on the amplitude of the transverse oscillations. The RFQ parameters were chosen to accept the central dense area of the initial energy-phase distribution into the separatrix corresponding to a particle moving on the axis. However, there are particles with large transverse amplitudes. These particles are captured for acceleration and have large amplitudes of longitudinal oscillations and form a halo in the longitudinal phase space. The total longitudinal emittance can significantly exceed the emittance of the central part containing 80 – 85% of particles. An obvious way to weaken the coupling between the transverse and longitudinal motions is to increase the injection energy and operate at lower frequency. Our present design addresses these issues by using 100-keV source voltage and 57.5-MHz injection frequency. The particle distribution simulated to the exit of the RFQ is used for the further beam dynamics studies in the superconducting section of the driver linac.

Electromagnetic fields of low-β SC resonators

The simulation of beam dynamics in the presence of all components of both electric and magnetic field is essential in superconducting quarter-wave resonators (SC QWR). The driver linac will use ~80 QWRs operating at 57.5 MHz and 115 MHz. Electrodynamics studies of the field distributions in the beam-cavity interaction area indicate appreciable dipole components of both electric and magnetic fields, especially for higher-frequency cavities. There is, however, another problem in QWR drift-tube design caused by quadrupole terms in the transverse Lorentz force which can cause appreciable emittance growth when the linac lattice includes transverse focusing by SC solenoids. Solenoidal focussing provides a compact lattice and maximizes transverse acceptance while maintaining low longitudinal emittance. Early SC resonator designs for accelerating heavy-ions included large diameter drift tubes to provide axial symmetry of the electric field in the beam aperture. Some recent QWR designs

eliminate the drift tube, perforating the cylindrical central stems. The reduced cylindrical symmetry around the beam axis introduces an appreciable quadrupole component of transverse rf field. Detailed analysis shows that the transverse effect of electric field in the accelerating gap can be represented as a sum of axially symmetric and quadrupole lenses. Rf field properties of several geometries of QWR and Half Wave Resonators (HWR) and the impact of field asymmetries on beam quality were studied by computer simulations of beam dynamics in realistic three-dimensional electromagnetic fields. Beam parameters were analyzed for several typical examples of accelerating-focusing lattice. We found that beam steering due to the dipole component of the rf field and emittance growth due to the quadrupole field component in the aperture can be largely avoided by the appropriate design of the SC resonators.

Focusing lattice design in sc linacs

In SC linacs, focusing elements alternate with accelerating cavities. In the design of the periodic focusing lattice of the SC linac, several important issues should be taken into account. Standard criteria such as stability of the transverse motion and maximum possible acceptance certainly should be applied. In SC linacs, due to the high accelerating gradients available from SC cavities and the relatively long focusing periods, strong interactions between transverse and longitudinal motion may occur. Long focusing periods containing several cavities per period decrease the cost of the accelerator. However, in some lattice designs, the transverse-longitudinal coupling can excite a parametric resonance of transverse oscillations. The condition for parametric resonances of transverse motion is fulfilled if the frequency of transverse oscillations is equal to a half-integer number of the frequency of longitudinal oscillations. This type of resonance condition can be a limiting factor to the total

voltage provided by a SC cavity, especially in the low-velocity section of SC linacs.

In the design of SC linacs, parametric resonances in transverse motion must be identified and avoided. The transverse emittance growth of the beam is more pronounced for larger longitudinal emittances. The parametric resonance can result in the formation of beam halo in transverse phase space if appropriate measures are not applied. In the RIA driver linac baseline design, a transverse phase advance in the range 60°-80° is recommended for the DTL. A transverse phase advance close to 90° is preferable in the elliptical cavity section. The results are valid for the selected lengths of the focusing periods of the RIA driver linac. Similar analysis techniques should be applied for different structures of the focusing period in SC linacs.

Stripper sections

In order to avoid beam losses in the high-energy section of the Driver Linac, the low-intensity unwanted charge states must be carefully separated and dumped. As long as the driver linac is designed for acceleration of multi-q beams, the beam transport system following the stripping foil must provide simultaneous matching of selected charge states to the six-dimensional acceptance

of the following SRF linac. This magnetic transport system (MTS) requires dipole magnets and a rebuncher in order to provide a proper transformation of the 6-dimensional beam emittance. The system has a dispersive area, effectively operating as a spectrometer. In the region of maximum dispersion, the unwanted charge states are removed by horizontal beam

collimation. We designed such systems for both stripping areas. We studied higher-order effects on the multi-q effective emittance in the MTS. Four sextupoles located in dispersive areas of the MTS were implemented in order to correct higher-order effects. The code COSY was applied for higher-order optimization of the MTS. To minimize the transverse

emittance growth the beam is focused to the spot of 2-mm diameter at the location of the stripper. Final verification and optimisation has been carried out by the help of TRACK code. Careful optimization allows us to avoid any emittance growth of the multi-q beam transporting through the MTS.

Design of the high-β section of the driver linac using triple-spoke cavities

Spoke-loaded cavities offer several advantages compared with the higher frequency elliptical cavities that were proposed for this range of particle velocities. For example, the triple-spoke cavities can provide operation at 4.5 K, broader 'velocity acceptance' of the transit-time factor (TTF), more accelerating voltage per cavity, and, in the RIA application, provide 'beam-loss-free' acceleration. A detailed comparative study of the beam dynamics in the elliptical cavity linac (ECL) operating at 805 MHz and in the triple-spoke cavity linac (TSCL) operating at 345 MHz for the application in high-β section of the RIA driver linac was carried out. In the case of ECL the frequency jump results in lower longitudinal acceptance as an consequence of

abrupt reduction of the phase width of the stable area in longitudinal phase space. In addition, due to the narrow 'velocity acceptance', the energy acceptance of the separatrix is low as well. Figure III-1 shows longitudinal acceptances for ECL and TSCL at the injection energy 81 MeV/u for $^{238}U^{89+}$ ion beam. Beam dynamics simulation included a careful design of the accelerating-focusing lattice of both ECL and TSCL linacs, the effect of carbon stripper with the thickness of 15 mg/cm^2 on the particle distribution and random errors of accelerating fields. The simulations show that the TSCL linac has a wide margin in energy acceptance to avoid any particle losses in the high-β section of the driver linac.
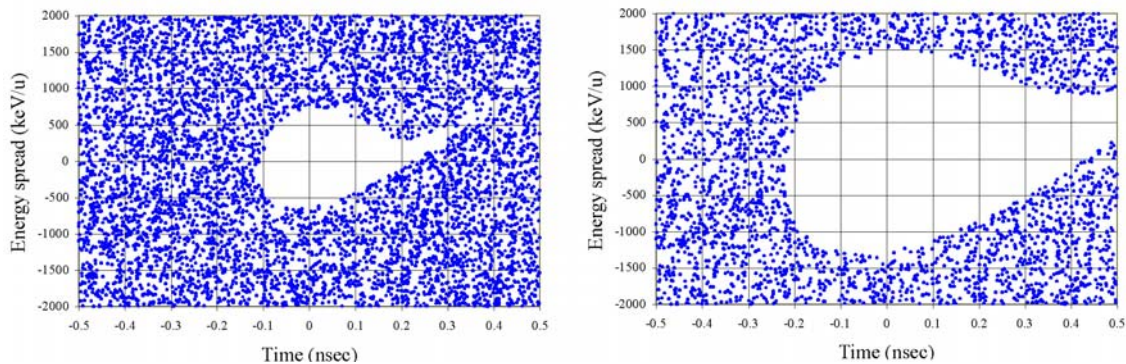

Figure III-1. Longitudinal acceptance of 805-MHz ECL (left) and 345-MHz (right) TSCL linacs shown in the same scale.

Beam dynamics in the post-accelerator

The section of the Radioactive Ion Beam (RIB) linac after the carbon stripper was conceptually designed for the acceleration of multiple-charge-state beams to enhance the available beam intensities for experiments. As was shown, a wide range of the charge spread Δq/q, about 20%, can be accepted and accelerated in the ATLAS accelerator. For the future RIB acceleration in ATLAS, we restricted the possible range of Δq/q to ≤11% in order to avoid emittance halo in the phase space. As a consequence of multiple-charge-state acceleration the total stripping efficiency is

significantly higher than for the single charge-state beams, as can be seen in Fig. III-2. The RIB linac of the RIA Facility will produce beam intensities more than an order of magnitude higher than post-accelerators based on an ECR charge breeder. However, the transverse and longitudinal emittances of multi-q beams will be larger by a factor of ~3 as shown by beam measurements in ATLAS. ATLAS will require modifications of the bend regions for the effective acceleration of multi-q radioactive beams.
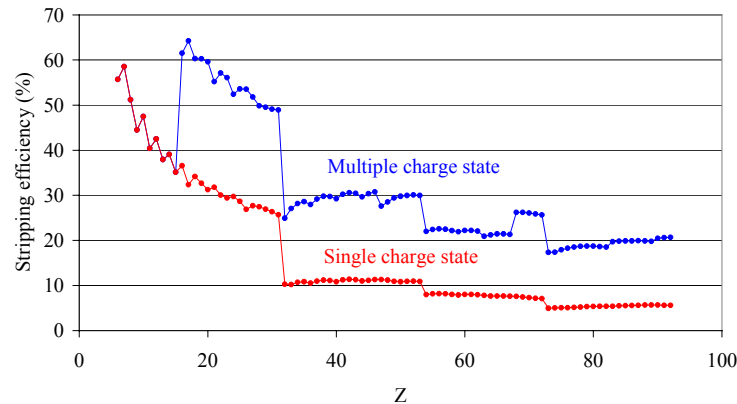
Figure III-2. RIB linac overall stripping efficiency in the regime of single and multiple charge state beam acceleration.

a.2.   Beam DynamIcs Optimization in the Driver Linac: Current Developments
(E. Lessner and P. Ostroumov)

Use of multiple-charge states impose strict requirements on the steering procedure to avoid effective emittance growth. A program of detailed beam dynamics studies was initiated to simplify the accelerator design, enhance its performance, and develop specifications for the engineering design of the accelerator systems. As part of the program, two research items are being investigated:

- Development of a new fitting code based on realistic field distributions in solenoid magnets.
- Development of steering methods and algorithms with realistic solenoid- field distributions. Refinement of steering methods that utilize combined-field solenoids including dipole coils.

1.   Beam matching in the focusing lattice must be done with realistic field distributions in the solenoids Existing fitting codes do not include realistic field distributions in solenoids. Preliminary calculations of the matched beam parameters are based on fitting codes like TRACE. This code is based on transport matrices and assumes "rectangular" distribution of the magnetic field in solenoids. The simulation code TRACK can represent solenoids as a "matrix" or can integrate particle motion through the solenoid using realistic field distributions. We found significant differences between the TRACE fitting and TRACK in the low-energy section. We are developing a fitting code that includes 3D field distributions. One of the new optimization code features is the calculation of the defocusing effects for every cell of the SC RF cavities, especially important in the low-energy section of the linac.

2.   Frequent steering correction of multiple-charge-state beams is extremely important to avoid effective emittance growth. Several correction schemes are being studied. One scheme is the standard correction technique whereby the trajectory is minimized at the Beam Position Monitors (BPM). Another algorithm is based on the beam-based alignment technique whereby trajectory information from two or more different focusing configurations is used to correct component misalignments. Previously, we had proposed to develop combined-field solenoids that incorporate dipole steering coils. Preliminary studies showed that the steering coils do not produce non-linear effects on the beam. Additional studies will be done to design a correction algorithm that takes into account the actual beam rotation in the solenoid, which couples the horizontal and vertical beam motions, and to develop effective steering procedures of multiple-charge-state beams in the transverse phase space.

a.3.   Effects of Single Errors on the Prestripper Lontgitudinal Emmittance
(E. Lessner and P. Ostroumov)

A comprehensive study of partial effects of accelerating field random errors on the longitudinal beam parameters in the prestripper was performed using the code "elegant" *as an independent evaluation* ofthe prestripper linac beam dynamics simulations performed with the code TRACKL.   "elegant"[1] wasoriginally written to simulate electrons and was modified for simulation of two-charge state ion beams. In order to emulate heavy-ion dynamics, the electromagnetic fields and magnet component stranagths were mapaped such that:

$$E_e/(q_{HI}E_{HI}) = -m_e/(A_{HI} \text{ a.m.u.}),$$

where E_e and E_{HI} stand for the electron- and ion- field strengths, respectively; m_e is the electron mass, and A_{HI} is the ion atomic mass. Since space charge effects are negligible in the prestripper linac, simulation of a two-charge-state beam can be done sequentially, each equivalent electron bunch accelerated by fields whose strengths are given by the above mapping.   The simulation results were then transformed back to heavy-ion parameters.

Table III-1. 4rms emittance at the end of the prestripper linac under single random errors.

[1]Phase Error (degrees)	4 RMS Emittance	4RMS Emittance
	(π keV/u-ns)	(π keV/u-ns)
	Calculated Average over 200 Seeds	Calculated Average over 200 Seeds
0.3	2.17	2.23
0.6	2.36	2.51
0.9	2.70	2.93
Field Strength Error)%)		
0.3	2.18	2.22
0.6	2.34	2.47
0.9	2.66	2.87

---

[1]M. Borland, "elegant: A Flexible SDDS-Compliant Code for Accelerator Simulation," APS-LS-287, http://www.aps.anl.gov/techpub/Isnotes/Is287.pdf

Random rf phase errors and field strength errors for the two-charge state 28^+ and 29^+ of uranium beam were simulated at three error levels and for 200 distinct seeds. Table I shows the 4rms emittance at the end of the prestripper linac resulting from each error type. Figures.III-3 and III-4 show the accumulated longitudinal emittance versus error strengths, and the histogram of the emittance growth factor for 0.9% rms field strength error, respectively.
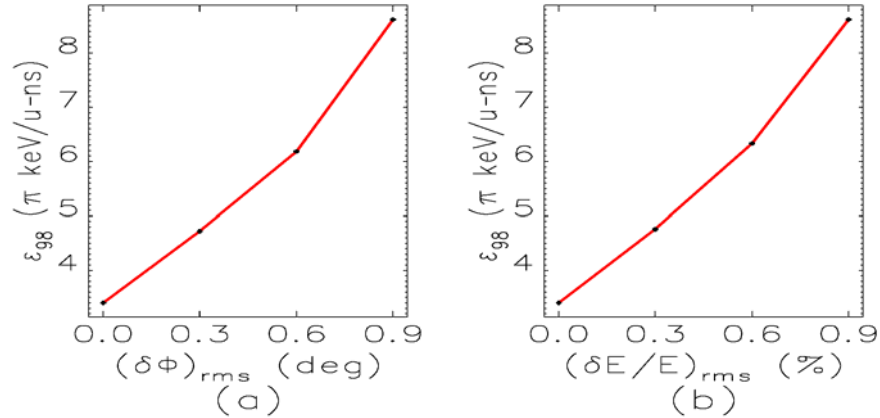

Figure III-3. Accumulated longitudinal emittance versus rf phase fluctuations (a) and accelerating field strength fluctuations (b). ε_{98} represents the superposition of the phase space areas at the exit of the prestripper linac, from which the distributions with the four largest areas were eliminated. The ε_{98} emittance, resulting from phase or field errors at the largest level, is of the order of 9 keV/u-nsec.

There were no particle losses at 0.9 ° rms phase error or at 0.9% rms strength error. The final distributions were well within the longitudinal acceptance of the low-β SRF linac.
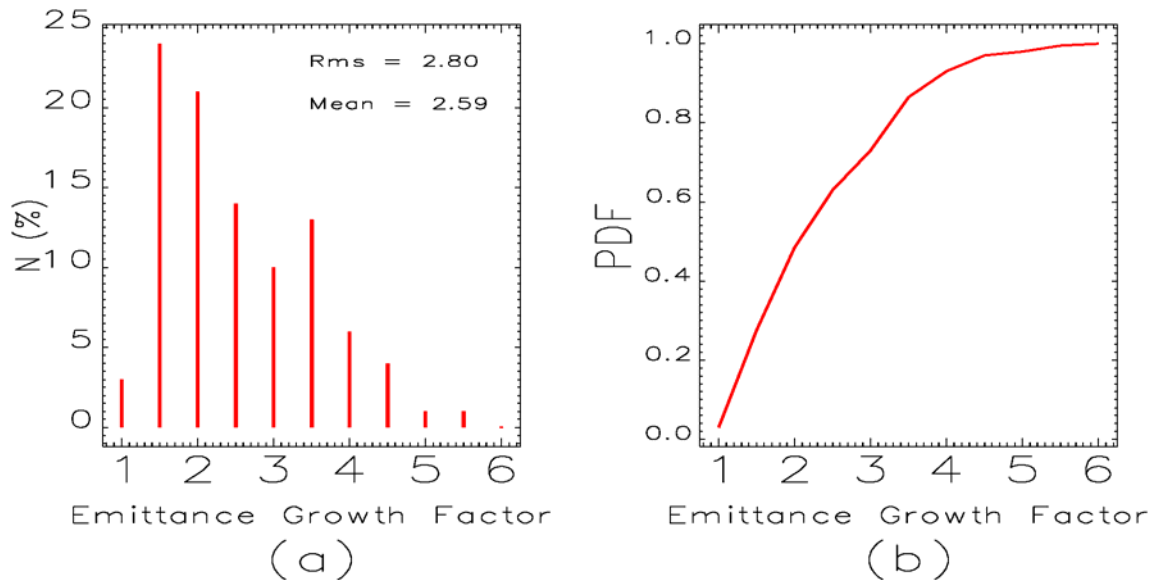

Figure III-4. Histogram (a) over 200 simulations of the emittance growth factor, defined as the ratio of the initial and final emittances for the 200 simulations, for 0.9% rms field strength errors, and the corresponding probability function (b). The frequencies are expressed in terms of the percentages of simulations resulting in the emittance values indicated. As can be seen, there is 98% probability that the emittance growth factor be less than 6.4.

a.4. A New Generation of Superconducting Solenoids for Heavy-ion Linac Applications (P.N. Ostroumov, S. H. Kim[*], E. S. Lessner, K. W. Shepard, R. E. Laxdal,[†] and R. Wheatley[‡])

For low- to medium-energy beams, drift spaces between accelerator components can cause effective emittance growth. An assembly of steering coils mounted on focusing solenoids is proposed that reduces drift spaces between resonators. Preliminary design studies were conducted on a 9-Tesla magnet (see Fig. III-5) to determine the feasibility of achieving high field, low fringe field, and integral dipole field, into one compact package. The assembly, including terminals, switches, and protection circuit, are designed to fit inside a 25-cm diameter helium reservoir and its overall length is 28 cm.

The bucking coils are sufficiently strong to minimize the stray field at distances greater then the physical length of the solenoid. The coils produce a low field region of less than 0.1 Tesla between 15 and 18 cm from the magnet centre. The geometrical configuration of the steering coil (see Fig. III-6) can be saddle-shaped, racetrack or circular (ring-shaped).
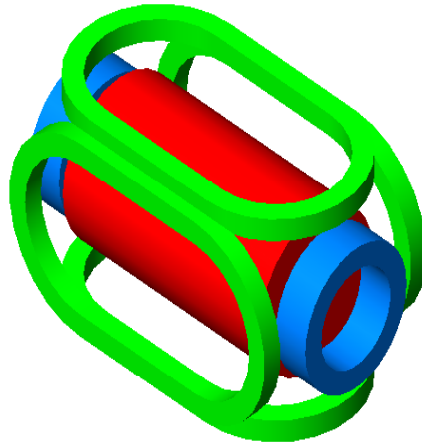

Figure III-5. Magnet assembly, showing solenoid, bucking coils, and racetrack steering dipole coils. The dipole coils generate 0.2 Tesla on the horizontal and vertical axes.

Parameters for the Racetrack Coil

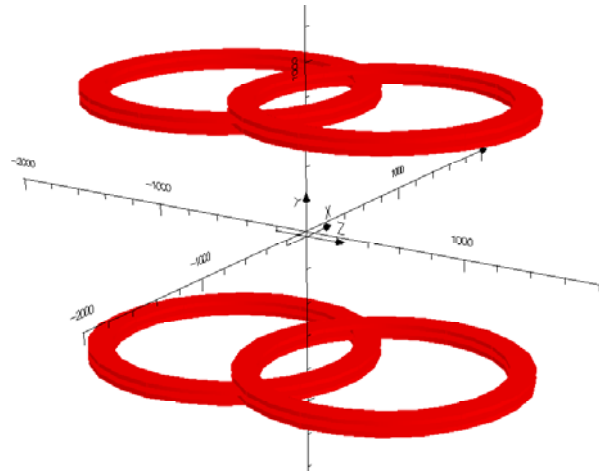|	
Straight Section (cm)	12
Total Length (cm)	28
Coil Diameter and Vertical Separation (cm)	14.8
Central Magnetic Field (T)	0.2 @ 31.7 kA
Field Integral on the Beam Axis (T-mm)	47.2

Figure III-6: Optional four-ring coil configuration with a radius of 7.7 cm and an overlap of 5.4 cm.

The steering coils can introduce non-linear effects on the beam dynamics. Numerical simulations were performed with the tracking code TRACK to determine the beam response to the realistic (3-D) magnetic field distributions including the steering coils. The steering algorithm corrects the horizontal and vertical beam slopes, x'_0 and y'_0, but not the beam displacements. For slope correction, both the horizontal and vertical slopes, as well as the beam-centre displacements, must be measured at the entrance of the solenoid/dipole assembly, due to the beam axial rotation in the solenoid (see Fig. III-7). The steering-field strength is set to the strength necessary to correct the beam slope calculated at the end of the solenoid with the dipole current turned off. Results are from simulations on the first part of the medium-β section of the SC driver linac, downstream of the first stripper.
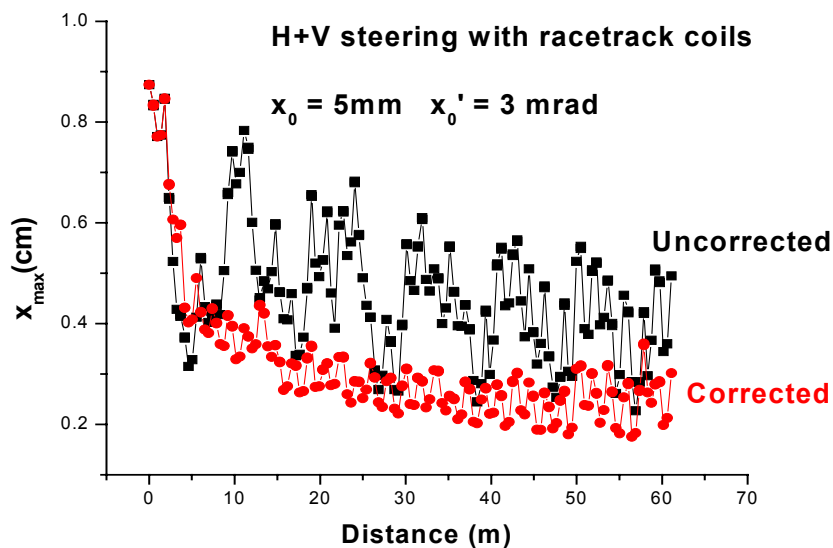

Figure III-7. Horizontal envelope for the five-charge-state uranium beam, before and after steering correction. 20,000 macro particles were used in the simulations.

∗XFD, ANL
†TRIUMF, Vancouver, B.C. V6T 2A3, Canada
‡American Magnetics Inc., Oak Ridge, TN 37831-250

Summary of the Normalized Transverse Emittance in the Horizontal Plane at the Entrance and Exit of the Lattice

Beam	One-charge-state		Five-charge-state	
Emittance (cm-mrad)	4-rms	Total	4-rms	Total
No Error (a) (b)	0.0593 0.0599	0.1145 0.1161	0.0593 0.0601	0.1145 0.1332
Uncorrected Error	0.0593 0.0597	0.1145 0.1175	0.0593 0.3633	0.1145 0.6906
Corrected Error	0.0593 0.0597	0.1145 0.1161	0.0593 0.0761	0.1145 0.2077

Initial Value   (b) Final Value

The emittance growth for the corrected five-charge-state beam comes from the multiplicity of charge states (see Fig. III-8). The steering coils do not produce non-linear effects on the beam. The beam distortions are negligible and well within the large lattice aperture of 3.0 cm. Further studies will include the solenoid-induced coupling in the steering algorithm.
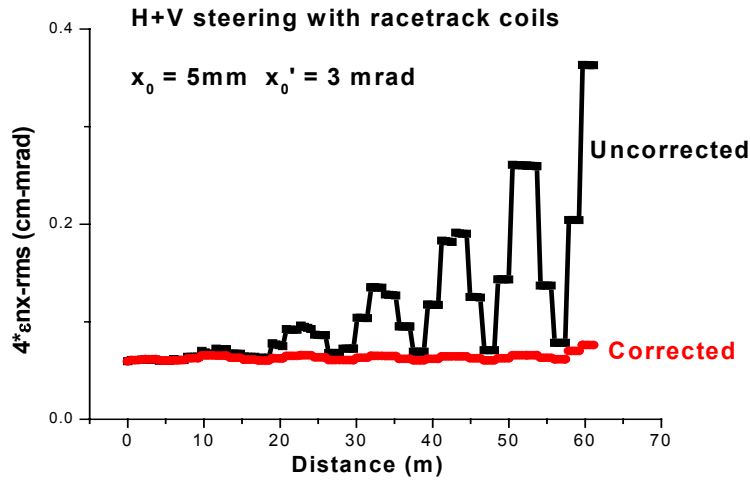

Figure III-8. 4-εn-rms emittance for the five-charge-state uranium beam. After correction, the emittance is reduced by a factor of three.

B. HEAVY-ION LINAC TECHNOLOGY

b.1. Prototype Quarter-Wave and Half-Wave Drift-Tube Resonators (K. W. Shepard, M. Kelly, J. Fuerst, and M. Kedzie)

Prototype construction was started for two types of drift-tube cavity which will be initially used to upgrade the existing ATLAS linac. The cavities are a 109-MHz QWR cavity and a 170-MHz half-wave resonant cavity which together can provide useful acceleration over a velocity range of 0.12 < v/c < 0.5. Figure III-9 shows cutaway views of the two cavities, which are approximately one meter in vertical extent. Both cavities are contained in an integral, stainless-steel helium vessel. Construction of both cavities is expected to be complete in FY2003.
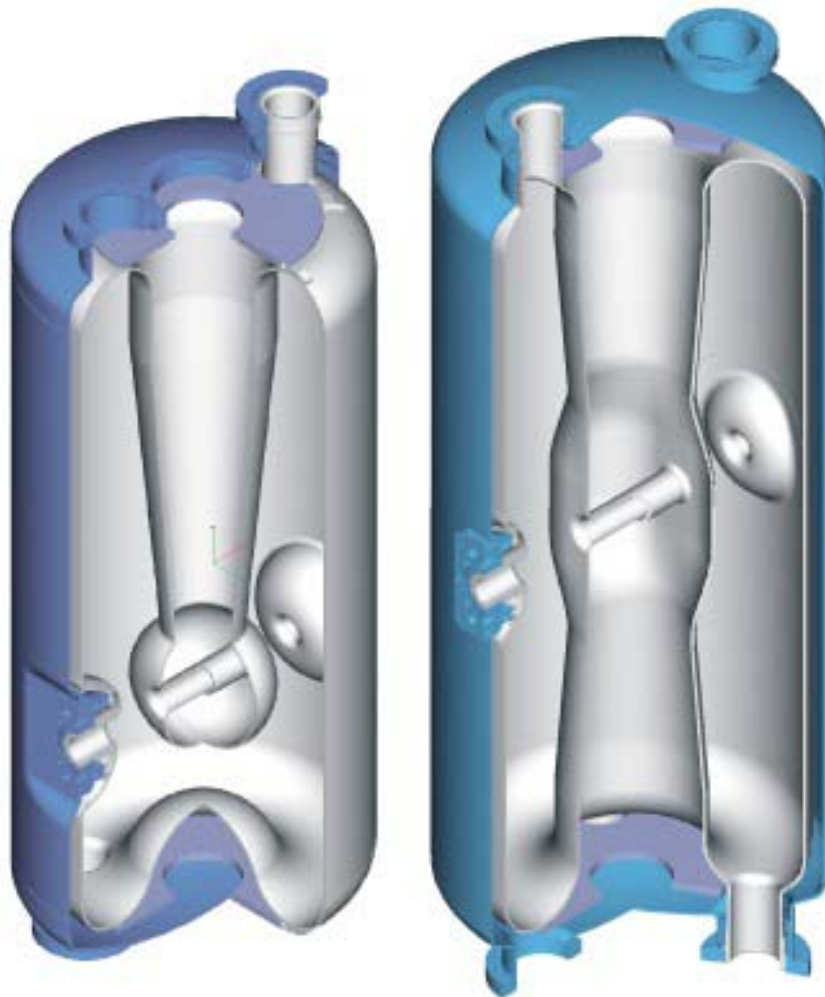

Figure III-9. Cutaway views of the quarter-wave and half-wave cavities showing both the niobium cavity shell and the integral stainless-steel outer helium vessel.

b.2. Prototype Cryomodule for Drift-Tube Resonators (K. W. Shepard, M. Kelly, J. Fuerst, and M. Kedzie)

Design of a prototype cryomodule for the above cavities is well-advanced. The cryomodule will provide separate vacuum systems for cavity (beam) and cryogenic vacuum. This will enable clean-room assembly of cavities, beam-line elements, and rf couplers, as detailed in Figure III-10. The end walls of the vacuum vessel are chamfered in the middle to allow room-temperature, low-particulate beam-line vacuum valves which seal and isolate the cavity-string assembly, to insert through the cryomodule vacuum wall.
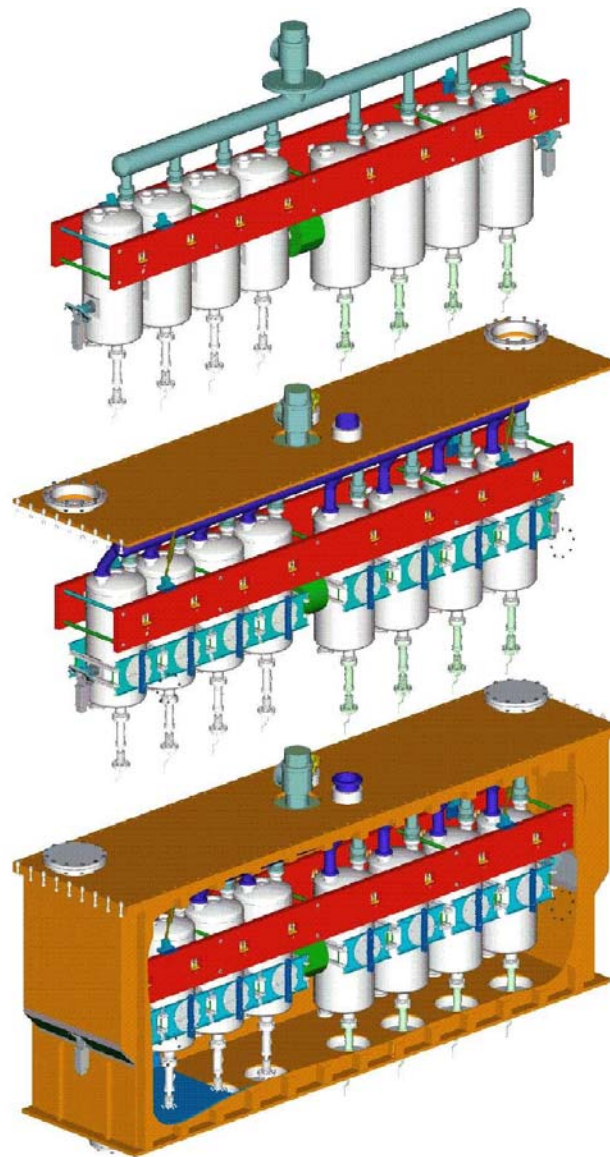

Figure III-10. Cryomodule assembly sequence. (Top) clean-room assembly of cavity string includes cavity and beam line vacuum and couplers. (Middle) Top flange assembly includes cryogenic systems. (Bottom) Completed cryomodule.

b.3. Prototype Double-Spoke Resonator (K. W. Shepard, M. Kelly, J. Fuerst, and M. Kedzie)

Construction of a prototype 2-spoke loaded 345-MHz superconducting cavity is nearing completion. The 3-cm aperture cavity, shown in Fig. III-11, has a useful stance of a multi-cell spoke cavity, and continues the development of spoke cavities that began with 350-MHz single-spoke cavities.of =0.29 and =0.4

successfully tested at ANL previously. The niobium elements of the cavity assembly are shown in Fig III-12, just prior to the closure welds that join the end-caps to the central, spoke-loaded section. Electromagnetic parameters for the two-spoke cavity are listed in Table III-2.
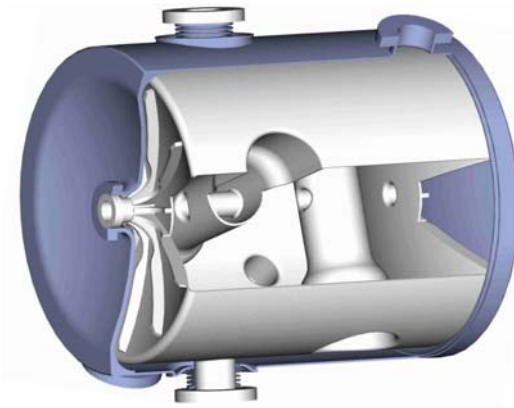

Figure III-11. Cut away view of a 345-MHz two-cell spoke cavity. The niobium housing diameter is 48 cm and the active length is 39 cm.
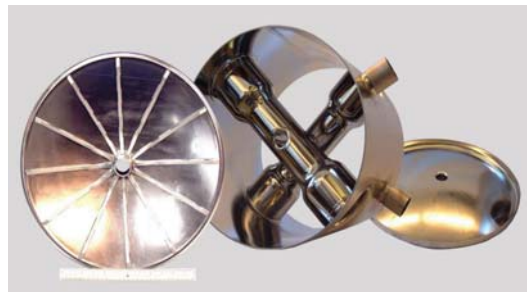

Figure III-12. Three pieces of the two-cell spoke cavity after receiving a heavy electropolish.

Table III-2. RF parameters for the β=0.4 two-cell spoke-loaded cavity.

frequency	347.072 MHz
Active Length =	-
$\beta_{Geom} =$	0.393
$QR_S =$	71
$U_o^* =$	151 mJ
$E^*_{peak} =$	3.47 MV/m
$B^*_{peak} =$	69 G

b.4.   **Hybrid RFQ Cold Model** (P. N. Ostroumov, A. Barcikowski, B. Rusthoven, S. Sharma, N. E. Vinogradov, and G. Zinkann)

The Hybrid Radio Frequency Quadrupole (H-RFQ) is an accelerating structure designed to accelerate low-velocity heavy ions with a q/A ratio = 1/240. The unique design of this low-frequency (12.125MHz), low-velocity accelerating structure enables it to be used as an efficient front end injector for a RIB linac. The H-RFQ structure consists of 3 sections of drift tubes and 2 RFQ sections. In the drift tubes sections the beam is accelerated and defocused transversely. Transverse focusing is provided by the RFQ sections. Each of the RFQ sections consists of two sets of non-modulated vanes with a length βλ separated by a drift space βλ/2. The appropriate focusing strength is achieved by adjusting the distance between the vanes. Using the combination of the drift tube and RFQ structures, a factor of two higher output beam energy, as compared to a regular RFQ accelerator, is achieved.

A half-scale (24.25MHz) aluminum cold model of the Hybrid RFQ was designed, built and tested. The goals were to determine the final resonator dimensions, accelerating and focusing field distribution, quality factor and coupling to the external power supply. First, a numerical simulation of the cold model's electrodynamic parameters was done using MWS code. The numerical simulation of this complicated structure had some difficulties. The size of the drift tube gaps and the RFQ vane spacing is very small compared to the overall dimensions of the cavity. This difference required a very large number of mesh cells for the simulation which resulted in unacceptable calculation time and the solution was non-convergent. To rectify this, some simplification of the shape of the structure had to be implemented. Even for $\sim 2 \cdot 10^6$ mesh points, just a few cells for each drift tube and only one cell for each RFQ gap were simulated.   The result is an estimate rather than a precise calculation of the electrodynamic parameters.   With this estimate frequency error in the simulation was expected. The frequency tuners which are used in the real model were not considered in the MWS model due to the same problem. Therefore, the designed resonator dimensions needed experimental testing and the aluminum cold model of the H-RFQ (Fig. III-13) was built.

The experimental investigation of the 24.25 MHz H-RFQ cold model was carried out using both an HP Network Analyzer and standard bead-pull technique using a phase-lock-loop. The first measurements of the electrodynamics parameters of the cavity revealed three important shortcomings of the cold model. These are: the measured quality factor turned out to be 3.5 times lower than the calculated value, the frequency was approximately 2 MHz high, and there was a tilt in the field amplitude distribution of the third drift tube section. The Q error can be explained by a poor rf contact between the vertical stems and the moveable plates of the frequency tuners. The low precision of the MWS simulation was considered as the reason for the other drawbacks.

The sliding rf contacts of the model were provided by a special spring rf gasket. The gasket material was purchased at Bal Seal Engineering. We observed that the Q of the cavity varied by factors of two when these sliding tuners were adjusted. It was realized that the contacts were at fault. A stronger spring material from the same firm was used to improve the rf contact. In conjunction with the stronger gasket material, special conductive silver grease, supplied by Tecknit, was employed. After these modifications were made, the measured quality factor was stable and was about 70% of the calculated value. Table III-3 summarizes this result.

To improve the resonant frequency, the dimensions of the H-RFQ model were changed. Cylindrical insertions to lengthen the vertical stubs of the cavity were designed and installed to lower the eigenfrequency. After this modification the resonant frequency was close to the expected value as is seen from Table III-3.

To improve the final problem of the field distribution tilt (Fig. III-14), capacitive tuners were installed at the required locations. These tuners removed the field tilt in the end of the third drift tube section.

The main goals for the near future are to make the field distribution uniform all along the structure axis and to measure the transverse field distribution in the focusing RFQ sections.

Table III-3. Resonator parameters.

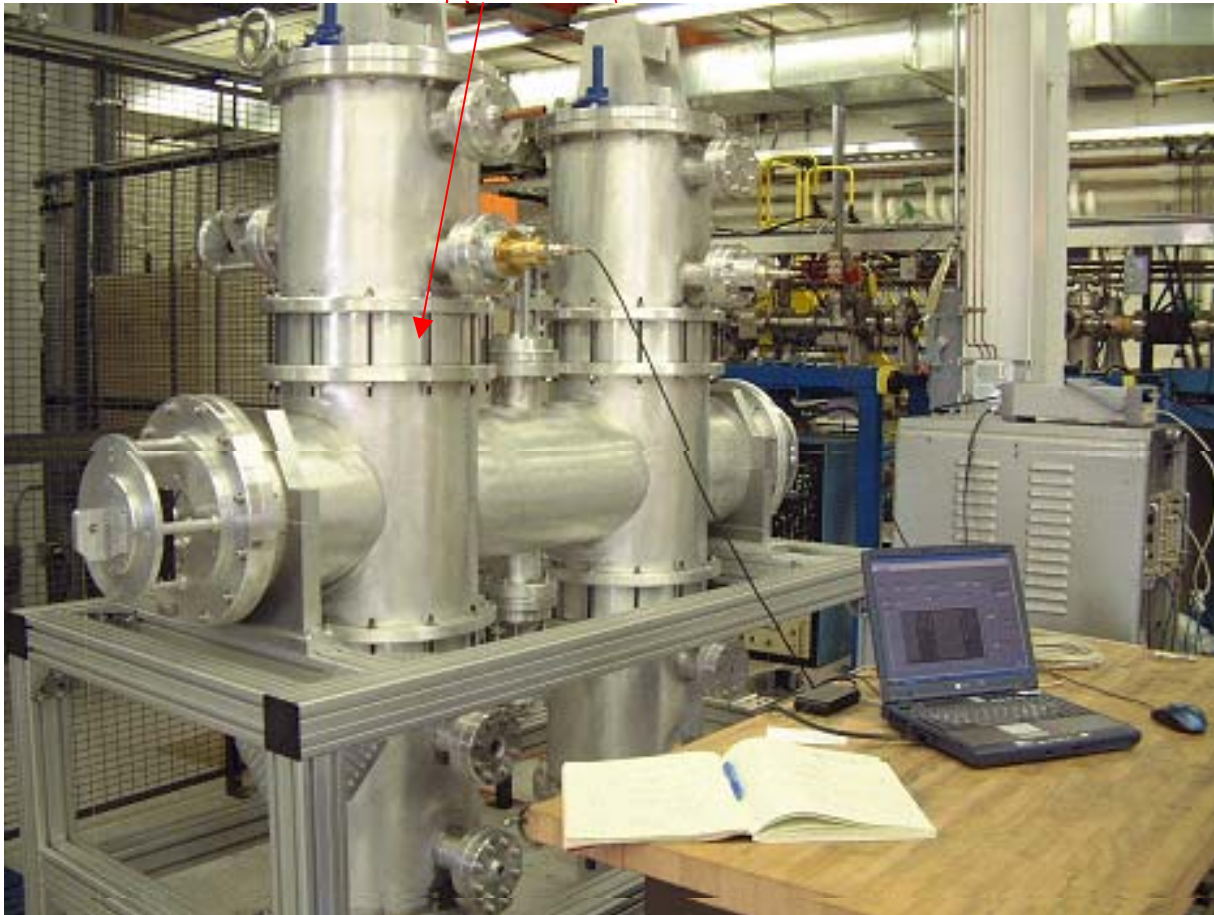|	MWS simulations	Before cavity modification	After cavity modification
Quality factor	4701	1350 - 2300	3360
Resonant frequency	24.65 MHz	26.5 MHz	24.25 MHz

Cylindrical insertions

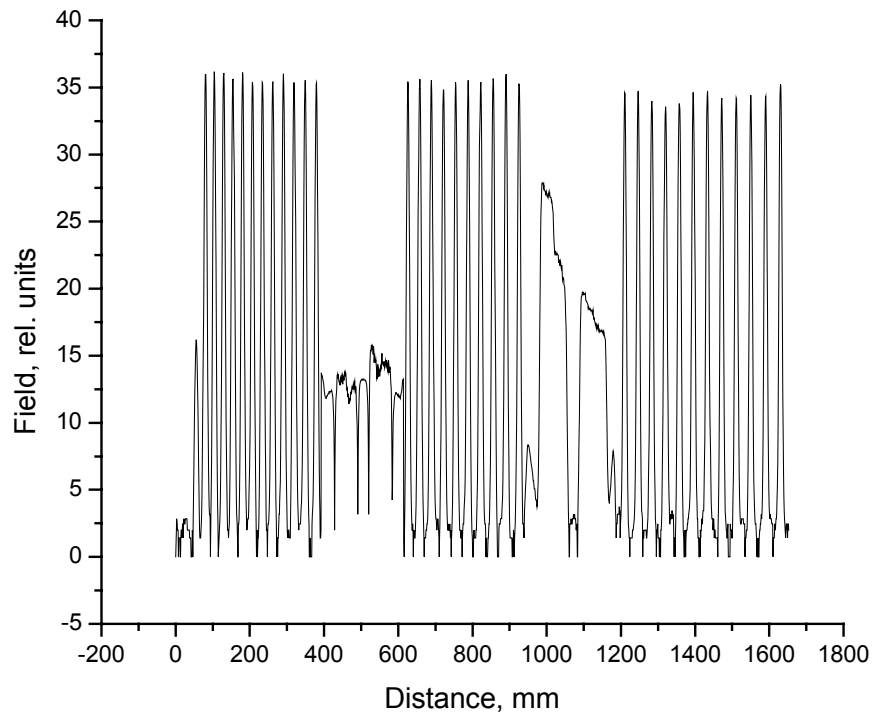*Figure III-13. The Hybrid RFQ half-scale aluminum cold model.*

Figure III-14. Bead-pull measurements of the electric field distribution along the structure.

b.5.   Engineering Design of 57.5 MHZ CW RFQ for the RIA Driver Linac

(P. N. Ostroumov, A. Barcikowski, F. DePaola, A. A. Kolomiets, J. W. Rathke,[*]
E. Rotela, B. Rusthoven, S. Sharma, D. L. Schrage,[†] and T.J. Schultheiss[†]

A Continuous Wave (CW) Radio Frequency Quadrupole (RFQ) accelerator is being designed for the Rare Isotope Accelerator (RIA) Driver Linac. This device is required to accelerate a wide variety of ion species as well as perform simultaneous acceleration of multiple charge states. As such, the structure must operate over a wide range of RF power dissipation from ~0.65 kW to 48 kW. The physics design of this pseudo split-coaxial RF structure was established earlier. The design addresses the requirements for efficient cooling throughout the structure, precise alignment, reliable RF contacts, and fine tuning capability. The RF, thermal and structural analyses werecompleted in response to these requirements. An RF analysis was used to determine the heat loss distribution on the cavity's internal surfaces. The heat loads were then transferred to a thermal model of a single segment and scaled to match total heat loss obtained from the code CST Microwave Studio. The thermal model includes the cavity vanes, walls and all cooling channels. To determine the coolant temperature rise, one-dimensional pipe flow elements were used. These elements account for fluid heat transport and heat transfer coefficients. The model was then used to minimize coolant flow by connecting the shell coolant channels in series. Temperature distributions were used as input to the structural model to determine stress levels and vane displacements. Different power levels were assessed as well as the thermal and structural response to vane-shell coolant temperature differences, which may be used to tune the resonant frequency. Results of these analyses show that the thermal and structural design of this RFQ is very robust.

A typical segment with cutaway sections to show the cooling passages is shown in Fig. III-15. Several different approaches to fabrication of the RIA RFQ were discussed during the conceptual design phase. Ultimately we have chosen a fully brazed assembly using step brazing to fabricate the vanes and quadrant details and finally a complete segment with end flanges.   This approach borrows heavily from the techniques used successfully on the LEDA RFQ at Los Alamos. The RFQ is designed as a 100% OFE copper structure with SST end flanges. For the simplicity of machining, fixtures and post-brazed handling for the vanes will be made from Glidcop. Six longitudinal segments will be mechanically assembled to form the complete 4-meter RFQ structure.

The aluminum cold model of the RFQ segment was designed and constructed. This model is necessary to verify final internal dimensions of the RFQ prior to the fabrication of full cooper structure, testing of machining and final assembly tolerances. An aluminum vane was used for the test of gravity force effect on the horizontal vane profile. Precise measurements for the gravity deflections of the vane show acceptable deviations of the vane's profile. The final assembly of the aluminum model is in progress. An aluminum vane photograph is shown in Fig. III-16.

A full power engineering prototype of a single segment of the 57.5 MHz RFQ is being developed. The main reasons to proceed with fabrication and testing of the engineering model are: a) the transverse dimensions of the RFQ are significantly larger than those in 4-vane high-frequency RFQs built using the brazing technique; b) due to the large cut-out in the vane, it is prudent to demonstrate mechanical stability during high temperature brazing. Once the fabrication is complete, testing of the RFQ prototype over the wide range of input power is necessary. Successful testing of the RFQ over the wide range of rf power level will simplify the design and minimize the cost of the RIA Driver Front End: the same RFQ will be able to accelerate full range of ions from proton to uranium. Currently we perform pre-tests of major brazed junctions of the RFQ engineering prototype. Figure III-16 shows the OFE copper vane prepared for the brazing.
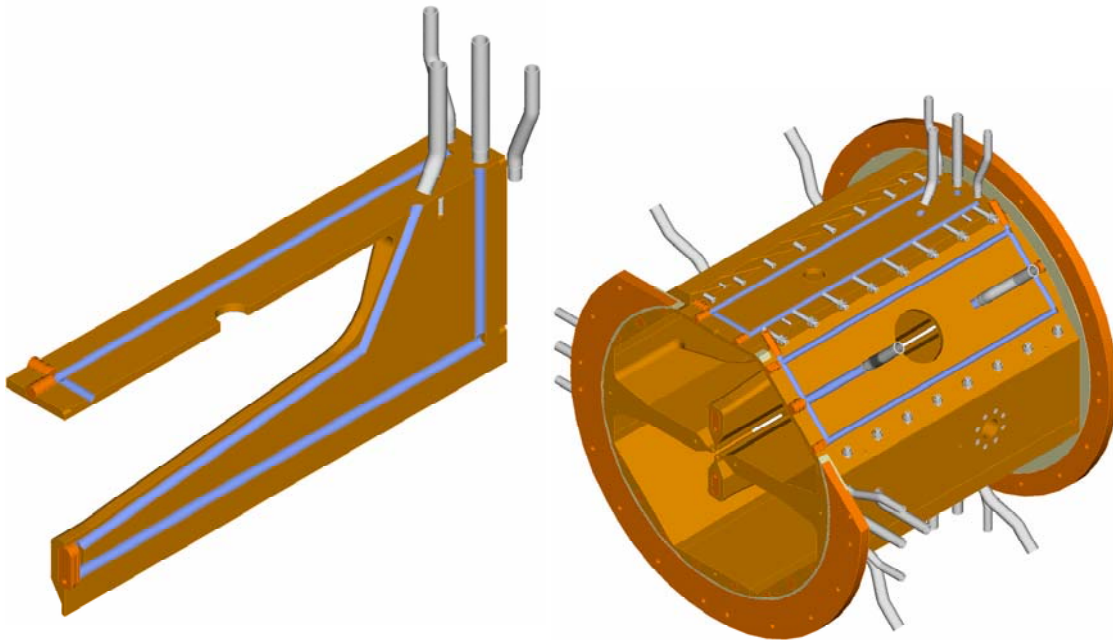

Figure III-15. Segment details with cooling channels. The vane assembly is shown separately on the left.
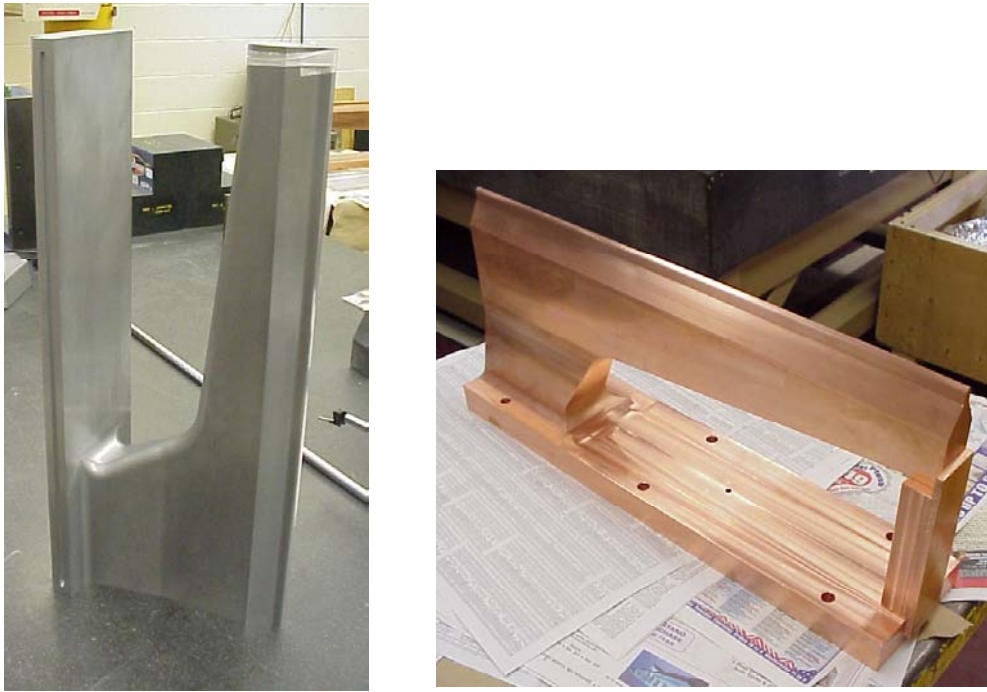
Figure III-16. Photographs of the aluminum (on the left) and copper (on the right) vanes.

C. RARE ISOTOPE PRODUCTION, SEPARATION, AND DIAGNOSTICS

c.1.   Development of Windowless Liquid Lithium Targets for Fragmentation and Fission of 400-KW Uranium Beams (J. A. Nolen, C. B. Reed[*], A. Hassanein[†], V. J. Novick[*], P. Plotkin[*], and J. R. Specht

Introduction

This section summarizes the on-going development of windowless liquid lithium targets being carried out for the RIA project. The goal of this work is to develop a fragmentation target that can easily work with uranium beams at least up to 100 kW and preferably up to 400 kW, the design limit of RIA. A schematic layout of the proposed concept is shown in Fig. III-17 and the performance goals for the target are listed in Table III-4. The beam-spot width is limited to 1 mm due to the optical requirements of the fragment separator. The target thickness is set by matching the energy loss of the beam with the acceptance of the fragment separator.

Thermal calculations for the full power RIA target

For a 400 MeV per nucleon uranium beam at a power of 400 kW the power density in lithium is 4 MW/cm^3, as indicated in Table III-5. For a graphite or beryllium target this would be about 15 MW/cm^3 due to their higher densities. With the lithium flowing at 20 m/s the power density is reduced by a factor of 20,000 keeping the maximum temperature below 300 C and the vapor pressure of the lithium at the hot spot below 10^{-6} T. For a nozzle cross section 1.5-cm wide by 3-cm long the total volume flow rate would be 9 liters/s and the average temperature rise would be 6 C.

Pressure/flow requirements and pump design for a prototype target

As a first step towards the design and construction of the full-sized windowless liquid-lithium target for RIA, a scaled-down prototype has been designed and is currently under construction. The prototype will have a thickness in the range of 1-2 cm and have a flow rate of 5-10 m/s.

_____

*Nuclear Engineering Division
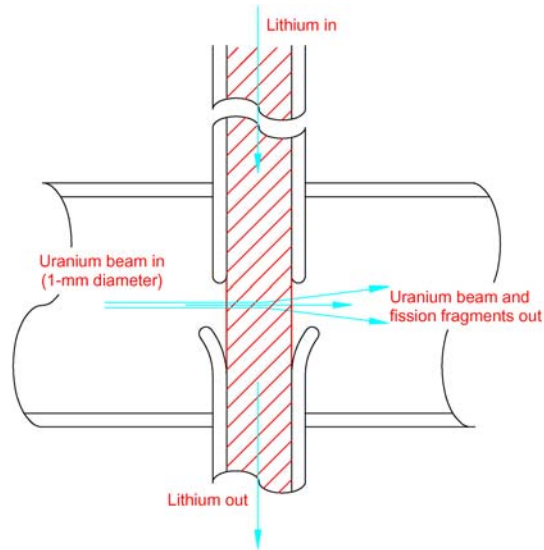[†]Energy Technology Division, Argonne.

Figure III-17. Schematic layout of the concept of a windowless liquid lithium target for in-flight fission or fragmentation of heavy ions up to uranium, designed to work with beam power as high as 400 kW.

Table III-4. Target requirements for uranium beam.

Beam energy:	400 MeV/u
Beam power:	400 kW
Beam diameter:	1 mm
Target thickness:	1.5 g/cm^2

Table III-5. Thermal properties of the target.

Beam energy deposited:	120 kW
Power density at no flow:	4 MW/cm^3
Power density at 20 m/s:	200 W/ cm^3
Hot-spot temperature:	300 C
Maximum lithium vapor pressure	10^{-6} T

Goals of this prototype project are to evaluate the lithium flow properties for a variety of nozzle types and to check the performance of our permanent magnet liquid metal pump designs. A drawing of the first nozzle to be tried is shown in Fig. III-18. It is rectangular at the output end to increase the target thickness while minimizing the lithium volume flow-rate required.

A DC, permanent magnet Lorenz-force type of pump was chosen for this liquid-lithium loop. It is a larger version of the pump designed for the hybrid beryllium/lithium target described previously.   To achieve the higher volume flow rate at the correspondingly larger pressure drop required for the windowless target a rectangular pump duct is being used. A sketch of the pump duct and its corresponding equivalent electrical circuit is shown in Figure III-19. A photograph of the pump duct is shown in Figure III-20. The stainless steel duct was fabricated via a wire electric-discharge-machining process from a solid metal block to avoid possible problems with cracking and corrosion in weldments that have been experienced previously in pumps with cold-worked ducts.
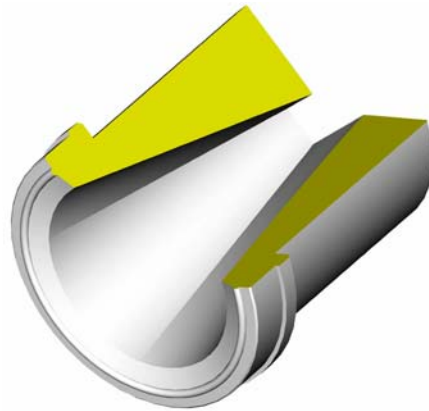

Figure III-18. A section view of the tapered nozzle to be used in the prototype liquid-lithium target. It is rectangular, 10 mm by 5 mm, on the output and circular, 22 mm in diameter, on the input.
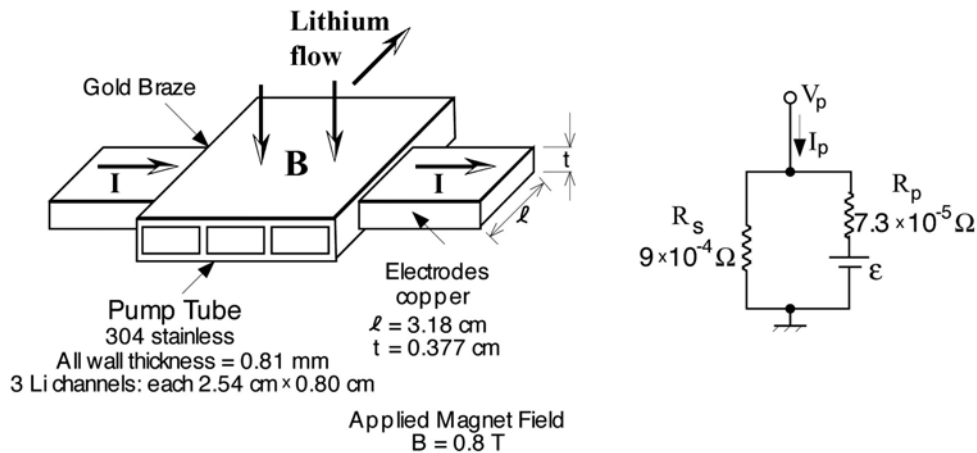

Figure III-19. Sketch of the DC permanent magnet pump concept and the equivalent electrical circuit of the pump duct.

Figure. III-20. Photograph of the pump duct and current electrodes for the prototype target.

The pump duct and plumbing of the liquid lithium loop are designed such that the pressure drops on these components are small relative to that at the pump nozzle. For the pump duct dimensions shown in Figure III-18 and nominally 5-cm piping, the pressure overall pressure drop of the system is calculated to be 30,000 Pa at 10 m/s nozzle velocity. With 0.75 T magnetic field the required pump current is 391 amperes at 71 mV. The total pump power is 28 watts, with 53% of this going into pumping lithium and the rest dissipated in the pump duct resistance.

Mechanical layout

A mechanical drawing of the liquid lithium loop is shown in Figure III-21. The lithium flows from the nozzle which is just above the center line of a standard 15-cm conflate vacuum cross.   There are clamp-on heaters and thermal insulation added to what is shown in the drawing.   A photograph of the partially assembled system is shown in Figure III-22.
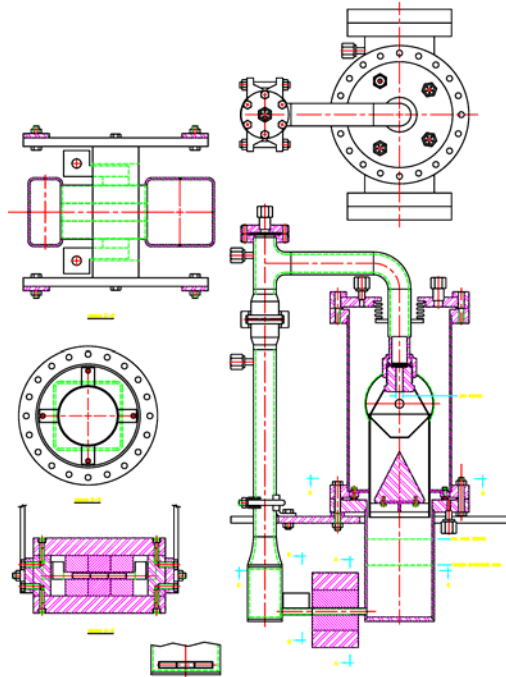

Figure III-21. Mechanical drawing of the liquid lithium target loop. The overall height of the loop is 0.6 m. A section view of the permanent magnet pump is shown at the lower left.
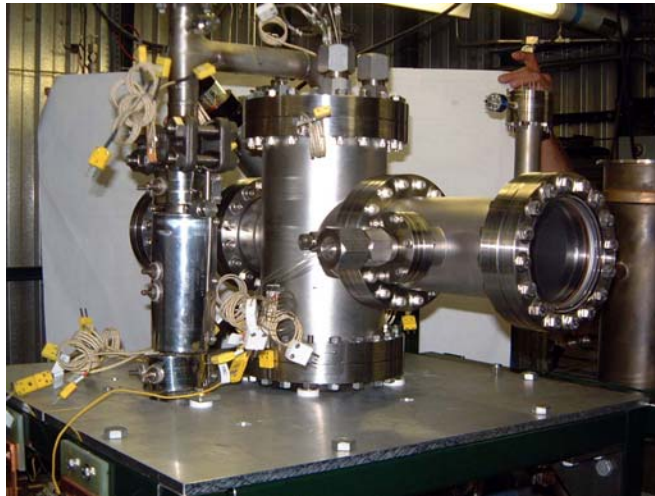
Figure III-22. A photograph of the partially assembly target system.

Safety issues and procedures

A general discussion of the safety procedures that are used for working with alkali-metal systems was given in Ref. 1. Specific procedures were written for the safe operation of the present system for initial testing within the existing liquid lithium laboratory at Argonne. These include a general safety document, a document of procedures for initial commissioning and operation of the loop, and a procedure to be followed for loading of the lithium into the pump loop.

Construction and testing

The mechanical and electrical components of this prototype system were fabricated and/or procured, the vacuum system leak checked after assembly, and the heaters and their controllers installed and debugged prior to loading the lithium. Approximately 760 g of lithium were loaded under an argon atmosphere and the assembly initially operated at atmospheric pressure with argon before commissioning under vacuum. Three runs were completed by the end of FY02 and 12 runs were completed by the end of CY02. The test runs provided evaluation of the pump design and flow characteristics relative to the design parameters, as well as the observation of the uniformity and stability of the lithium jet as a function of flow velocity. Alternative nozzle designs were also evaluated. Smooth, steady jet flow was observed for all anticipated nozzle velocities, up to roughly 10 m/s of lithium jet velocity, which corresponds to approximately 900 A of pump current. Next year's goal is to demonstrate operation of the system on-line at high beam power in a 40 kW beam on target dynamitron test rig at ANL.

The full-scale RIA liquid-lithium target requires scaling this prototype up by a factor of 3 in thickness and a factor of 2 in velocity. After the addition of a heat exchanger, the only additional sub-system to be incorporated for long-term operation at high intensity will be one for impurity control. Impurity control traps, both hot and cold, were developed as part of the inertial fusion materials irradiation developments. These methods were shown to provide for control of radioactive impurities such as tritium and ^{7}Be, as well as, carbon, nitrogen, and oxygen.

[1]J. A. Nolen, C. B. Reed, A. Hassanein, and I. C. Gomes, Nucl. Phys. **A701**, 312c-322c (2002).

c.2. Simulations of Effusion from ISOL Target/Ion Source Systems (B. Mustapha and J. A. Nolen)

In a previous work,[1] we reported on the implementation of a Monte-Carlo calculation to simulate the release process of radioactive isotopes from ISOL-Targets. In this calculation, the effusion process is simulated using the tool-kit Geant-4[2] by tracking the particles through the target until released from the ion source. The diffusion is treated analytically using the solution of Fick's diffusion equation[3] for the considered form of the target material: foils, fibers or grains. We have also shown that it is possible to characterize the release process and extract its important parameters, the diffusion coefficient (D) and the sticking time per collision (τ_s), by fitting the simulated release curve to the experimental one measured with a given target geometry for a given isotope. The extracted information can then be used to improve the efficiency of existing targets and design new geometries more suitable to produce beams of rare isotopes.

In the same study, the simulation of the whole release process (diffusion, effusion and decay) of ^{8}Li from the RIST target[4] tested online at ISOLDE-CERN has revealed that the diffusion coefficient D can be determined only if the diffusion process is faster than the decay of the considered isotope. To determine D when the decay is faster than the diffusion (case of ^{8}Li), we could use the value measured for the closest stable isotope (^{7}Li).

To better characterize the diffusion and effusion processes and avoid the uncertainty coming from the underdetermination of D, we propose here to deconvolute the two processes and study them separately. This will allow the unambiguous extraction of the release parameters from the appropriate measurements: τ_s from effusion measurements and D from diffusion measurements. It will also provide an independent benchmark of the effusion and diffusion parts of the calculation.

In this report, we focus on the study of the effusion part of the release process. The only parameter in this case is the sticking time τ_s. Furthermore, if we consider non-sticky particles ($\tau_s = 0$), noble gases for example, there will be no parameters at all and the problem is fully determined for a given geometry. Using effusion measurements for non-sticky particles, we can perform a direct and independent benchmarck of the effusion part of the calculation. The calculation will provide us with information like the total path length and number of collsions for a given geometry which could later be used to measure the sticking time of other particles.

We report here on the simulation of three Target/Ion Source systems used at Oak Ridge National Laboratory[5,6] to measure effusion times of different rare gases. Both low- and high-conductivity systems were used in these measurements. In the next section, the principle and the conditions of these measurements will be presented. In the next section, the results of the simulation of the low-conductivity systems will be presented and compared with the corresponding data. Some checks of the simulation using data for simple geometry components and using the conductance approach will be presented and discussed in the following section, followed by a comparison between the low- and high-conductivity systems based on the simulation. Our concluding remarks will be given in the last section.

Effusion measurements at ORNL

In these measurements, the considered gas is admitted to the system at a controlled rate through a needle-valve (see Figure III-23a) until a steady flow is reached. Then, a fast valve system closes the inlet in about 0.1 ms and the decay rate of the ion source current is measured, see Figure III-23b. The characteristic effusion time, τ_e, is determined by fitting the decay curve using an exponential form: \alpha exp(-t/ τ_e).
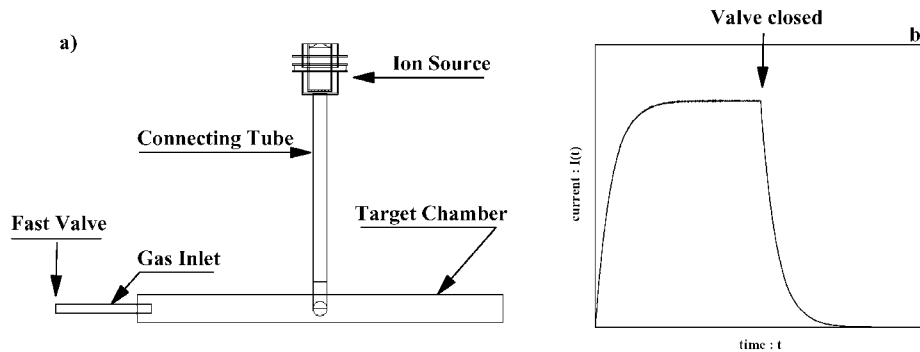

Figure III-23. Principle of ORNL measurements : a) A typical geometry used to measure effusion times (1st low-conductance system) showing all geometry components including the Gas Inlet/Valve system. b) A typical measured release curve showing the steady flow while the valve is open (the plateau) and the exponential decrease after the valve is closed.

The measurements were performed for different noble gases: He, Ne, Ar, Kr and Xe at different temperatures: 1073-1473 K. Two kinds of geometries were used: low- and high-conductivity systems. The low-conductivity geometry is characterised by small section tubes connecting the target chamber to the ionsource (see Figure III-24a). In the high-conductivity geometry, a more open connection is used (seeFigure III-24b).

For each geometry, the data were taken for both an empty target chamber and one filled with a Reticulated Vitreous Carbon Foam (RVCF) matrix. The simulation is performed only for the case of empty target chambers.

Simulation of low-conductivity systems

There are two low-conductivity systems for which effusion times were measured. They differ by the size of the target chamber. In the first (Figure III-23a), the target chamber was a 1.5 cm diameter and 19.3 cm long tube. In the second (Figure III-24a), a larger tube was used: 2.4 cm diameter with the same length. In both cases the target was connected to the ion source using an elbow (0.87 cm diamter, 3.5 cm total axis length) and a tube (0.87 cm diameter and 10 cm long).

The simulation of the first system (Figure III-23a) showed that particles travel on average 125 m before leaving through the ion source and collide about 11000 times with the internal surfaces of the system. The effusion time calculated for ^{4}He at 1473 K is 44.9 ms which is about twice the measured value ($\sim$ 23 ms). Trying to understand the extra delay in the simulation, we simulated the case without the ion source in order to estimate its contribution to the delay, the results are summarised in Table III-6.

Table III-6. Results of the simulation as the average number of surface collisions and total path length of particles for the first low-conductivity system (Figure III-23a) with and without the ion source. The calculated delay times for ^{4}He at 1473 K are compared to the measured value in the bottom line.

	W/ Ion Source	No Ion Source	Experiment
<N. collisions>	10987	4466	-
<Path length> (m)	125.3	90.3	-
τ (ms)	44.9	19.1	23.0

We notice that by removing the ion source, the simulation is faster than the data which seems to be consistent with the data because the ion source will introduce an additional delay anyway. The question now is: what is the real delay introduced by the ion source? Since we don't simulate the ionization process in the calculation, it is possible that we predict more delay than the experiment where particles could be extracted faster once ionised in the ion source. A possible precise measurement of the delay, introduced by the ion source, could be carried out by using a simple tube connected to the ion source instead of to the whole system.

The simulation of the second low-conductivity system (Figure III-24a) showed that on average particles travel about 300 m and collide about 15000 times before leaving the system. For ^{4}He at 1473 K, the calculated effusion time is 105.6 ms which is about 3 times the experimental value (~ 38 ms). And more surprisingly, even after removing the ion source the simulation predict more delay than the experiment, see Table III-7. This is of course inconsistent with the data and with the first geometry, because the argument of the accelerating effect of the ion source can't explain this discrepancy.
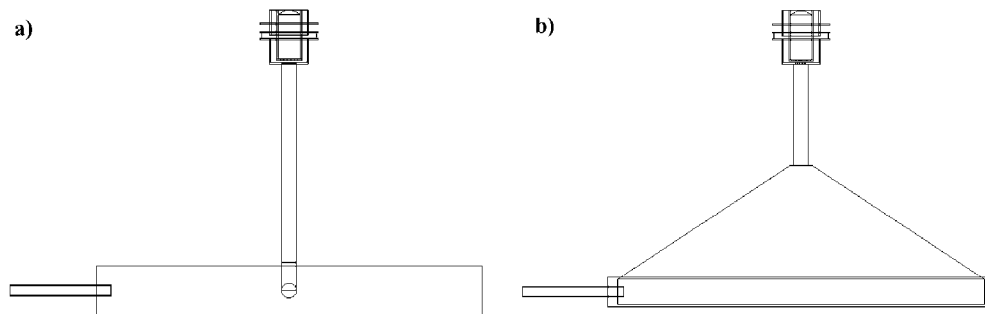

Figure III-24. Low- and high-conductivity systems : a) Geometry of a low-conductivity system (2nd low-conductivity system). b) Geometry of the high-conductivity system.

Table III-7. Results of the simulation as the average number of surface collisions and total path length of particles for the second low-conductivity system (Figure III-24a) with and without the ion source. The calculated delay times for ^{4}He at 1473 K are compared to the measured value in the bottom line.

	W/ Ion Source	No Ion Source	Experiment
<N. collisions>	15550	6540	-
<Path length>(m)	294.7	130.6	-
τ (ms)	105.6	46.8	38.1

The present conclusion is that the quantitative increase in the delay time calculated for the larger tube is in the right direction, but it is larger than seen experimentally. In order to find the source of this discrepancy, we performed some independent checks of the simulation. Tests using basic geometry components were carried out and confronted to experimental data. They are discussed in more detail in the next section.

Tests of the simulation

In 1960, Levenson et al.[7] reported on measurements of transmission probability of particles through simple shapes: tubes, elbows, etc. The measurements were performed by admitting a gas into one end of the considered shape and measuring the pressure at entrances and exits. The transmission probabilities from one end to another were then determined using the pressure difference.

After adapting the calculation to give the transmission probability, the simulation was performed for the tube and elbow shapes, the basic components of ORNL's systems. Tubes and elbows with different length-to-radius ratios (L/R) were considered. In the case of elbows, L is the total axis length.

Comparisons to the data are shown in Figure III-25a for tubes and Figure III-25b for elbows. We notice that the simulation agrees very well with the data within error bars. This test provides an important validation of the Monte Carlo simulations.
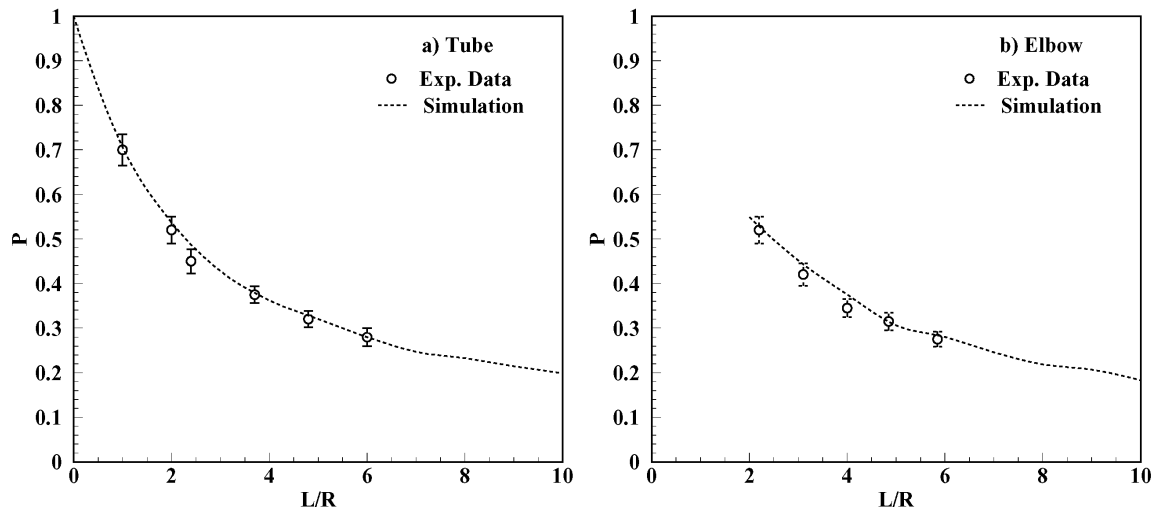

Figure III-25. Test of simulation using experimental data : a) case of a tube and b) case of an elbow. Open circles with error bars are data from[7] and dashed line is the result of the simulation.

This first test dealt only with transmission probabilities of particles through basic shapes and did not test the delay time predicted by the simulation. In order to check the timing from the calculation, we used the conductance approach well known in vacuum technology.

The problem of unsteady molecular flow through a long tube could be resolved by analogy to the one-dimension heat-conduction problem.[8] Consider the case of N_0 particles trapped between the two ends of a long tube (L >> R). At t = 0, one end of the tube is opened and particles start leaving the tube. This is of course a non steady flow of particles because the number of particles leaving the tube is varying in time until no particle is left inside the tube.

Based on the above analogy, the number of particles leaving the tube at a time t is given by :

$$N(t) = N_0 \times \frac{8}{\pi^2 \tau_0} \sum_{n=0}^{\infty} \exp(-(2n+1)^2 \frac{t}{\tau_0})$$

τ_0 is the characteristic delay time (effusion time) given by the following expression :

$$\tau_0 = \frac{4}{\pi^2} \frac{V}{C}$$

where $V = \pi R^2 L$ is the volume of the tube,

$C = \frac{2}{3}\pi \frac{R^3}{L} v$ is the conductance of the tube

assuming L >> R. $v = \sqrt{\frac{8kT}{\pi M}}$ is the average Maxwell velocity for a particle of mass M at a temperature T.

The simulation was run for $N_0 = 10^5$ particles using a 1 cm diameter and 100 cm long tube ($V = 78.5$ cm^3). The conductance calculated for ^{4}He at 1473 K is C = 730.8 cm^3/s resulting in a delay time $\tau_0 = 43.5$ ms. The value determined from the simulation is 42.8 ms, in a good agreement with the conductance approach.

The comparison of the simulated N(t) with the conductance formula is shown in Figure III-26. A very good agreement is seen except at longer times where the end effect of the tube manifest itself by liberating all particles at a finite time.
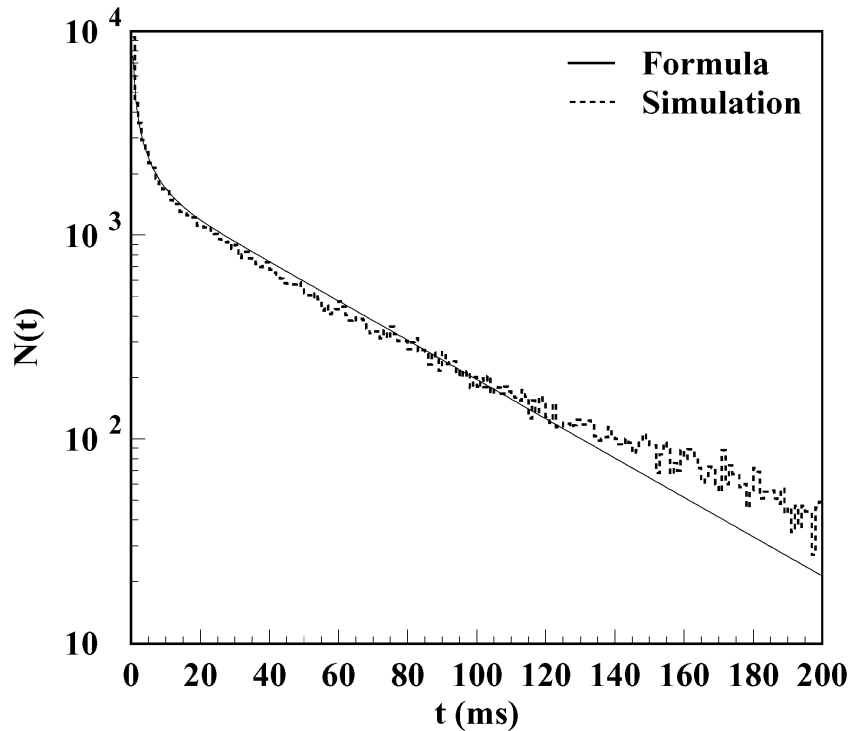

Figure III-26. Comparison of the simulation with the conductance approach for a long tube.

The simulation gives a delay time in good agreement with the conductance approach for a simple tube. We will now generalize this approach to the more complicated geometry of the low-conductivity systems used in ORNL's measurements.[5]

Because the geometry of the low-conductivity systems is essentially simple tubes with different lengths and sections connected to each other, it is possible to treat it like the serial coupling of these same tubes. In this case, the conductance C of the whole system could be obtained by :

$$\frac{1}{C} = \frac{1}{C_1} + \frac{1}{C_2} + \frac{1}{C_3} + ...$$

where 1,2,3,... denote the tubes. The total volume of the system is simply the sum of volumes $V + V_1 + V_2 + V_3 + ...$ The characteristic delay time in the system could be determined using the same expression for τ_0.

Applied to the two low-conductivity systems, this approach gave the results shown in Table III-8.

Table III-8. Comparison of the simulation with the conductance approach for the two low-conductivity systems.

	V (cm^3)	C (cm^3)	Conductance τ_0 (ms)	Simulation τ_0 (ms)	Experiment τ_0 (ms)
1st system	40.3	803.4	20.3	19.1	23.0
2nd system	97.0	856.9	45.9	46.8	38.1

We notice a good agreement between the simulation and the conductance approach for both geometries. Note that in Table III-8 neither the Monte Carlo simulation nor the conductance calculation include any delay from the ion source.

Comparison of low- and high-conductivity systems

The simulation of the high-conductivity system (Figure III-24b) showed that on average, particles travel about 355 m and collide about 22000 times inside the system including the ion source. The delay time calculated for ^{4}He at 1473 K is 127.3 ms which is more than 3 times the experimental value: 34.8 ms, see Table III-9. Simulating the case without the ion source gives a delay time of 33.5 ms which is smaller than the measured value. This result is consistent with the first low-conductivity geometry because the difference with the data could be explained by an eventual effect of the ion source.

The high-conductivity system was designed with more open geometry in the purpose of a faster release, but the experiment showed that the first low-conductivity system is faster. In order to understand the reason for that, we will use the conductance approach which gives almost the same results as the simulation.

Table III-9. Results of the simulation as the average number of surface collisions and total path legnth of particles for the high-conductivity system (Figure III-24.b) with and without the ion source. The calculated delay times for [4]He at 1473 K are compared to the measured value in the bottom line.

	W/Ion Source	No Ion Source	Experiment
<N. collisions>	221.55	5784	-
<Path length> (m)	355.5	93.5	-
τ (ms)	127.3	33.5	34.8

In the conductance approach, the delay time τ_0 is proportional to the ratio volume-to-conductance (V/C) of the system. So, in order to compare the conductance of two systems, we should consider the same volume V. In this case, the faster system is the one with the higher conductance C.   Comparing the high-conductivity system with a low-conductivity system having the same volume showed that the high-conductivity system is about 2 times faster than the low-conductivity one (71.1 ms for the low-conductivity case vs. 33.5 ms for the high-conductivity case). This confirms that using a more open geometry helps make the release faster. (Again the delay times are calculated without including the ion source.) However, the geometry of Figure III-23a is faster than that of the more open geometry of Figure III-24b, because it is dominated by the smaller overall geometry.

Concluding remarks

Monte-Carlo simulations of the low- and high-conductivity Target/Ion Source systems, recently tested at Oak Ridge National Laboratory, were performed. Compared to the experimental data, the simulation predicts more delay for all the systems. The simulation of the first low-conductivity and the high-conductivity systems without the ion source seems to give closer results to the data. However, the discrepancy seen for the second low-conductivity geometry can not be explained by an eventual effect of the ion source. On the other hand, the simulation seems to agree well with data measured for simple geometries and with the results obtained using the conductance approach well known in vacuum technology. The same conductance approach showed that the comparison of the low- and high-conductivity systems should be done for systems with the same total volume. In this case, the high-conductivity system is faster confirming the advantage of using more open geometries if the total volume is not increased.

At this stage, we consider that the simulation is partially validated. However, other verfications are needed. In collaboration with the ORNL's group, we propose special measurements to study the effect of the ion source. This could be done by replacing the target by a simple tube directly connected to the ion source. It will also be important to perform other measurements to confirm the data obtained for the second low-conductivity system.

[1]B. Mustapha and J.A. Nolen, Proceedings of the 14th International Conference On Electromagnetic Isotope Separators And Techniques Related To Their Applications, May 6-10, 2002, Vectoria, Canada, to be published in Nucl. Instr. and Meth. B.

[2]Geant4 home page : http://geant4.web.cern.ch/geant4/.

[3]"The mathematics of diffusion" by John Crank, Clarendon Press, Oxford, 1975.

[4]C. J. Densham et al, Nucl. Instr. and Meth. B 126 (1997) 154.

[5]J.C. Bilheux, G.D. Alton et al, Proceedings of the Particle Accelerator Conference, June 18-22, 2001, Chicago, Illinois.

[6]J.C. Bilheux, G.D. Alton et al, Proceedings of the International Conference on the Application of Accelerators in Research and Industry, Nov.12-17, 2002, Denton, Texas, to be published by AIP.

[7]L.L. Levenson et al, Proceedings of the 7th National Symposium on Vacuum Technology Transactions, American Vacuum Society, Oct. 12-14, 1960, Cleveland, Ohio.

[8]"Foundations of Vacuum Science and Technology", edited by J. M. Lafferty, John Wiley & Sons, 1998.

Once the simulation is validated using the experimental data from noble gases, the calculated total path length and number of collisions will be fully determined for a given geometry. This information could then be used to extract the sticking time of more reactive species in future measurements. Combined with the future diffusion measurements at the UNISOR facility at Oak Ridge, a complete release study of an important range of rare isotopes will be possible.

c.3.   Calculated Intensity of Secondary High-Energy Neutron Beams from Uranium and Deuteron Beams at RIA (B. Mustapha, J. A. Nolen and B. B. Back)

Neutron sources and beams are of great interest for both fundamental research and applications in other fields like material sciences and biological sciences. At the proposed Rare Isotope Accelerator (RIA), spallation and fission of high-energy (up to 400 MeV/n) heavy-ion beams will be used to produce secondary beams of exotic and rare isotopes. Along with these nuclei, many neutrons will also be produced. Knowing the intensity and the characteristics of such secondary neutron beams is important for possible applications. It is also important for radiation shielding purposes to know the energy and angle spectra of these neutrons.

We report here on the calculation of the flux of high-energy neutrons produced by the in-flight spallation-fission reaction of a 400 MeV/n ^{238}U beam in a liquid ^{7}Li target. The calculation was performed using a Monte-Carlo code based on the two-step model of Serber[1] for the spallation reaction: an Intra-Nuclear Cascade (INC) step[2] followed by an Evaporation or Desexcitation step.[3] More details on the calculation are presented in the next section. The results in the form of neutron's energy and angle distributions as well as the corresponding flux are presented in the following section. A comparison with the deuteron break-up reaction (a well-known source of neutrons) at the same energy on the same target is discussed in the final section.

Description of the calculation

In order to simulate the inverse kinematics reaction: 400 MeV/n ^{238}U + ^{7}Li target, the calculation was performed first for the direct kinematics: 400 MeV/n ^{7}Li + ^{238}U target, using an INC + Evaporation-Fission codes. Then a Lorentz transformation is used to obtain the result for the inverse kinematics case. No particle transport is considered in this calculation, which means that we are assuming that the target is extremely thin, i.e. neither the beam energy-loss nor the secondary reactions in the target are included. In order to consider these effects, we should run the calculation for different incident nuclei, fragments of the beam, at different energies, down to the beam energy after the target. We will discuss later how the beam energy-loss and the secondary reactions in the target affect the production of neutrons and their energy-angle distributions. In this section, the model on which the INC + Evaporation-Fission calculation is presented and the codes used will be described.

The spallation reaction is well described by the two-step model of Serber.[1] A first step, where the incident particle (usually a nucleon or light nucleus) penetrates the larger target nucleus inducing a cascade of inter-nucleon interactions, is called the intra-nuclear cascade. During this step some energetic particles are ejected, mostly nucleons, and an excited fragment called prefragment is left behind. The second step corresponds to the deexcitation of the prefragment by emitting slower particles or by fission in the concerned mass region. This step is called deexcitation or evaporation-fission. An intermediate step called preequilibrium[4] could also take place to bring the prefragment from its locally excited state to its thermal equilibrium and during which some intermediate-energy nucleons and light nuclei could be emitted. The preequilibrium step is not considered in this calculation.

For the intra-nuclear cascade step the code ISABEL of Yariv and Frankel,[2] which could be used to simulate nucleus-nucleus collisions, was used for the direct-kinematics reaction ^{7}Li (400 MeV/n) + ^{238}U . The second step was simulated using the deexcitation code ABLA of Schmidt et al.[3] The code ABLA includes

deexcitation by particle emission known as evaporation and by fission. After fission, the fission fragments could also evaporate particles. The emission of neutrons, protons and alpha particles is considered. No other composite particle emission is included. The results obtained for the direct kinematics are then transformed to the inverse kinematics case (RIA case) using the corresponding Lorentz transformation.

Results

After transforming to the inverse kinematics case, we obtained the result for the reaction 400 MeV/n ^{238}U + ^{7}Li. The result corresponds to a run of 10^5 interactions, in which about 2.7×10^6 neutrons are produced, 27 neutrons per reaction in average. Considering the reaction cross section ($\sim$ 5 barn), 11 neutrons are produced per incident ^{238}U nucleus on a 1 g/cm^2 ^{7}Li target. Considering a beam intensity of 1 pμA (100 kW beam power), 7.25×10^{13} neutrons are produced per second over all energies and angles.

The angular distribution shows that most of the neutrons are emitted into forward angles smaller than 7 deg, as Figure III-27(left) shows. The energy spectrum shows an important peak centered around the beam energy (400 MeV) with a $\sim$ 300 MeV width, see Figure III-27(right) showing the energy spectra for different angle intervals. This peak contains mainly the neutrons produced by the evaporation step. In the center of mass, the evaporation neutrons are isotropic and their energy peaks at $\sim$ 1-2 MeV. When transformed to the laboratory frame, these neutrons become forward-peaked with energies about the beam energy per nucleon (400 MeV). We notice also the absence of this energy peak at large angles. These neutrons are mainly produced in the intra-nuclear cascade step.
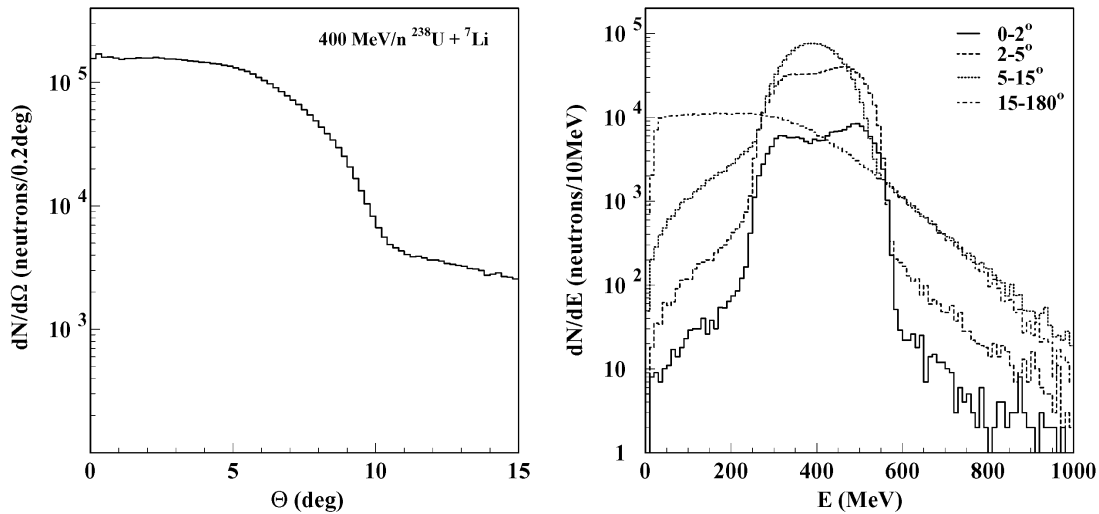

Figure III-27. Left- Angular distribution of neutrons from 10^5 spallation reaction of 400 MeV/n ^{238}U on a ^{7}Li target. Right- Energy spectrum for different angular intervals.

The peak asymmetry seen for θ < 5° is due to the fact that forward-emitted neutrons in the center of mass (higher energy in the Laboratory) are more likely to be within small Laboratory angles than the backward emitted ones. It is clear that neutrons in the energy peak are forward emitted in the laboratory frame and that those in the tail are emitted into large angles.

In order to consider the target thickness and study the effect of the beam energy loss on the neutron spectra, the 1 g/cm^2 target was considered as a set of 10 equal layers and by calculating the beam energy-loss using the code described in Ref. 5, we determined the incident energy on each layer. The beam loses about 9 MeV in each layer. The calculation was then performed at 10 different beam energies (from 400 to about 300 MeV/n)

on a 10 times thinner target 0.1 g/cm^2. The result showed that the neutron energy peak is slightly shifted towards lower energies. The angular distribution showed the same behavior but neutrons are slightly less forward focused. A reduction of about 5% in the total number of neutrons was also noticed. This effect is considered in the calculation of the neutron flux below.

Another important aspect of thick targets is secondary reactions. The effect of these secondary reactions was not considered in this calculation. However, we expect that secondary reactions will produce lighter final fragments that is usually due to the emission of more particles especially neutrons. Therefore, more neutrons will be produced, with energies lower than the primary neutrons energies. In this calculation we considered only neutrons produced in primary reactions, which gives a lower limit of the neutron flux.

From the angular distribution of Figure III-27(right) we can determine the corresponding neutron flux. For a 1 pµA - 400 MeV/n ^{238}U beam incident on a 1 g/cm^2 liquid lithium target, the central neutron flux exceeds 10^{11} neutrons/cm^2/s at 1 m downstream of the target and it is about 10^9 neutrons/cm^2/s in the central 1 m^2 at 10 meter, see Figure III-28(left). This is a very high flux for neutrons of such high energy ~ 400 MeV), see Figure III-28(right). The energy width of the forward peak is about 300 MeV.
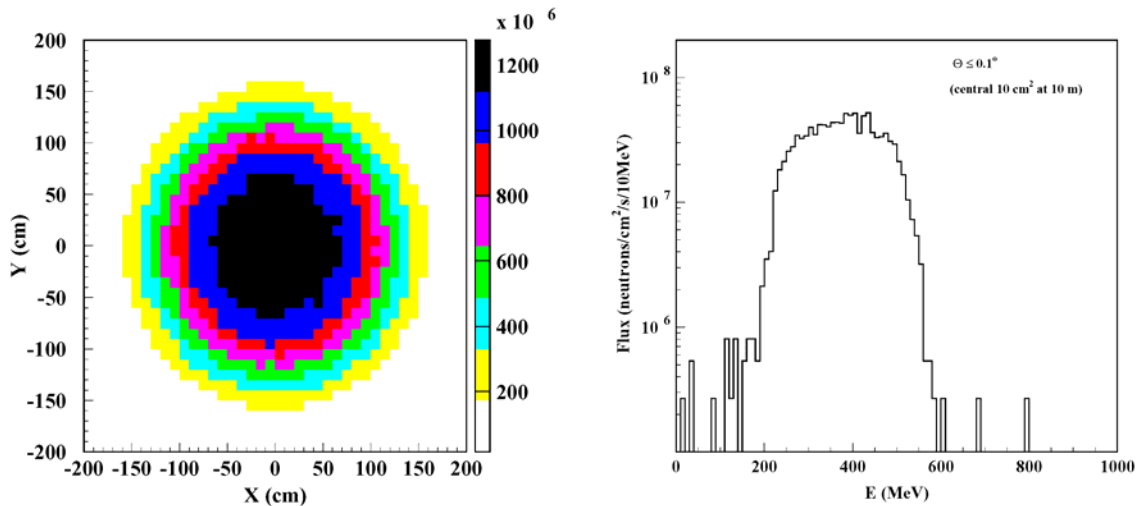

Figure III-28. Left- Neutron flux (neutrons/cm^2/s) at 10 m from the target. Right- Projection in energy of neutrons emitted at an angle θ < 0.1^o corresponding to the central 10 cm^2 at 10 m from the target.

Comparison to the deuteron breakup

Another important source of neutrons is the deuteron break-up reaction. In this section we calculate the energy-angle distribution of neutrons produced by deuteron breakup. For this purpose, we performed a calculation using the code LAHET[6] of the reaction of an 800 MeV (400 MeV/n) deuteron beam on a 5 g/cm^2 liquid-lithium target. The code LAHET considers the transport of particles in thick targets. 10^6 events were processed. The deuteron break-up cross section at this energy is about 200 mb, deduced from the measurement of ~ 1 GeV deuteron beam on a Be target.[7]

The angular distribution, presented in the left part of Figure III-29, shows that deuteron break-up neutrons are more forward focused than those from uranium reactions. This can be understood by looking at the right part of Figure III-29 showing the energy spectra for different angle intervals. The neutrons that are more forward focused, θ < 5°, have energies very close to the beam energy per nucleon. These neutrons were spectators in the reaction and have kept the direction and velocity of the beam, unlike the evaporation neutrons from uranium (forming the energy peak in the uranium case) that are isotropically emitted in the center of mass and focused by effect of the boost to the laboratory frame.
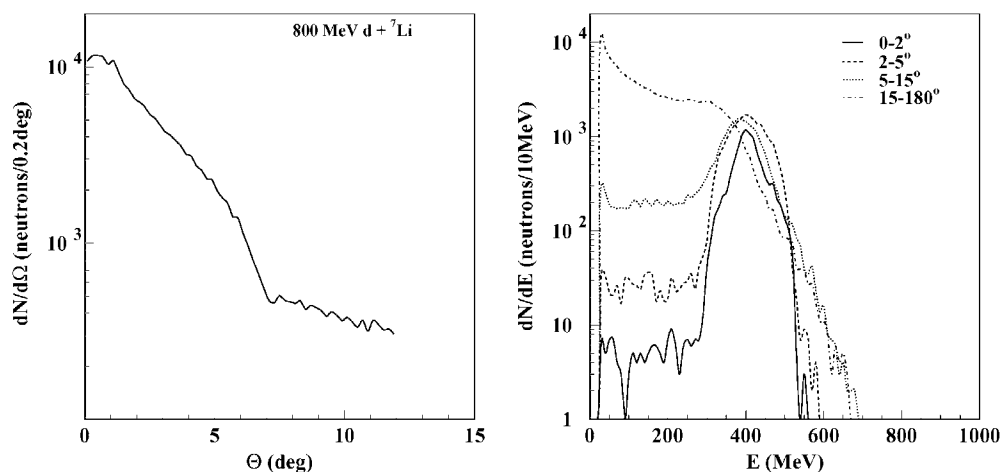
Figure III-29. Left- Angular distribution of neutrons from 10^6 deuterons at 800 MeV on a ^{7}Li target. Right- Energy spectrum for different angular bins.

The angular distribution shows that for an equivalent beam power, 100 kW, an 800 MeV deuteron beam on 1 g/cm^2 liquid ^{7}Li target produce half the neutron flux produced in the spallation of a 400 MeV/n uranium beam on the same target. But the energy distribution shows that forward neutrons from the deuteron break-up reaction have a better defined energy within a narrow peak centered about the beam energy per nucleon (400 MeV). Forward neutrons from the spallation reaction are more spread-out in energy as shown in Figure III-30. Therefore, more neutrons can be produced by using a thicker target in the case of

deuteron break-up without significantly altering their energy-spectrum. However, this is not true for the case of spallation. Figure III-30 compares the energy spectra of forward neutrons produced in the deuteron break-up in a 5 g/cm^2 ^{7}Li target and the spallation of ^{238}U on a 1g/cm^2 ^{7}Li target. In this case, the neutron flux from deuteron break-up is twice the one produced by spallation-fission of uranium. At zero degrees it is about 3×10^9 n/cm^2/s corresponding to a neutron energy peak at 400 MeV

_____

[1]R. Serber, Phys. Rev. 72 (1947) 1114.

[2]Y. Yariv and Z. Fraenkel, Phys. Rev. C 20 (1979) 2227.

[3]J.J. Gaimard and K.-H. Schmidt, Nucl. Phys. A 531 (1991) 709.

[4]J.J. Griffin, Phys. Rev. Lett. 17 (1966) 478.

[5]C. Scheidenberger et al, Nucl. Inst. Meth. B 90 (1998) 441.

[6]R.E. Prael and M.B. Chadwick, LANL Report NM-87545, 1997.

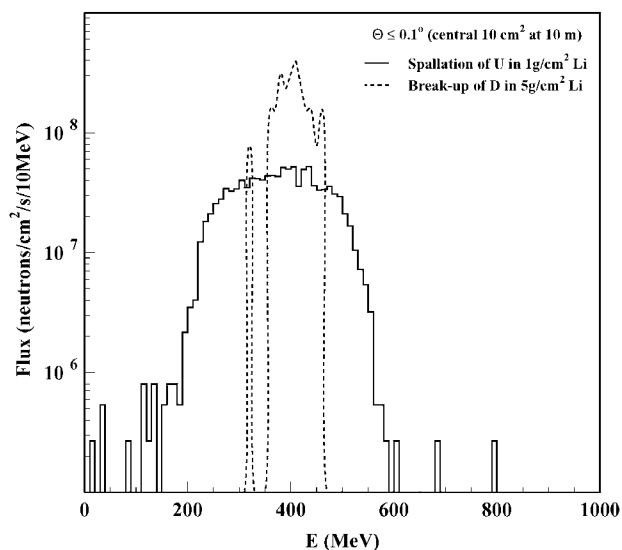[7]J.F. Lecolley et al, Eur. Phys. J. A 5 (1999) 321.

Figure III-30. Comparison for the same beam power (100 kW) of the neutron flux as a function of energy from ^{238}U spallation and Deuteron break-up on a liquid ^7Li target. The flux is calculated for the central 10 cm^2 at 10 m downstream of the target.

c.4.   Construction and First Tests of the Full-Scale RIA Gas Catcher Prototype

(G. Savard, T. Coccolios, A. Frankel, B. Blank, J. P. Greene, A. Heinz, A Levand, D. Seweryniak, W. Trimble, B.J. Zabransky, Z. Zhou, J. Clark[*], C. Boudreau[†], F. Buchinger[†], J.E. Crawford[†], S. Gulick[†], J.K.P. Lee[*], M. Maier[‡], K.S. Sharma*, J. Vaz[*], J.C. Wang[*], and the S258 Collaboration)

The ability to slow down and cool fast recoils from fragmentation or in-flight fission reactions with high efficiency is an essential component of the RIA concept. It is particularly important to produce reaccelerated beams of refractory and reactive elements. Standard ISOL techniques have difficulties with such elements while traditional IGISOL approaches do not provide enough stopping volume to efficiently accomplish this task. A new approach based on a large gas catcher system was developed to fulfill this task, a prototype built and an initial on-line test performed this year.

The design of the RIA gas catcher prototype was based on a smaller gas catcher, with a 7.6 cm inside diameter and a 25 cm length, which is working effectively at the front end of the Canadian Penning Trap (CPT) experiment at Argonne[1] where it cools both neutron-rich and proton-rich radioactive beams for high-efficiency injection into the CPT ion traps. The design of the smaller CPT gas catcher was essentially scaled up to obtain the first RIA prototype gas catcher ("the

big cell") designed to handle the range straggling of high-energy heavy-ion recoils and the angular straggling introduced by the final degrader and the window. Degraders in front of the entrance window remove all but roughly the last few MeVs energy per nucleon. Inside the catcher, the remaining energy is absorbed by ionizing room-temperature high-purity He at roughly 1/5 bar. Near-complete stopping of these ions is possible in .5 atm-m of He; the gas catcher aims to extract these ions efficiently.

These demands in stopping power determine the size of the big cell, a cylindrical gas volume 1.2 m long and 25 cm in diameter mated to a conical extraction cone. The construction of this large catcher was completed in the summer of 2002. 49 ring-shaped electrodes in the cylinder and 277 plates in the cone (see Figure III-31) provide DC bias for transport and extraction, and RF bias for focusing. Tuned circuits were constructed to provide the RF and DC fields to the cone and cylinder electrodes (Figure III-32). The catcher and the electronic circuits to apply the DC gradients and RF

fields were then installed inside a Faraday cage for high voltage safety.

Ions stopped in the gas catcher are pulled towards the cone, focused in the cone and extracted at the tip of the cone by gas flow through a 1.4 mm conical nozzle into an RFQ ion guide. The buffer gas is removed from the RFQ chamber by an Osaka TC440C helical groove pump with a Welch 1398 backing pump. DC electric fields extract the ions from the ion guide through a second nozzle into a vacuum system consisting of a time-of-flight line leading to a Si detector for activity measurement and a MCP detector for ion detection.

_____
[*]Department of Physics and Astronomy, University of Manitoba, Winnipeg MB R3T 2N2
[†]Department of Physics, McGill University, Montreal, PQ H3A 2T8
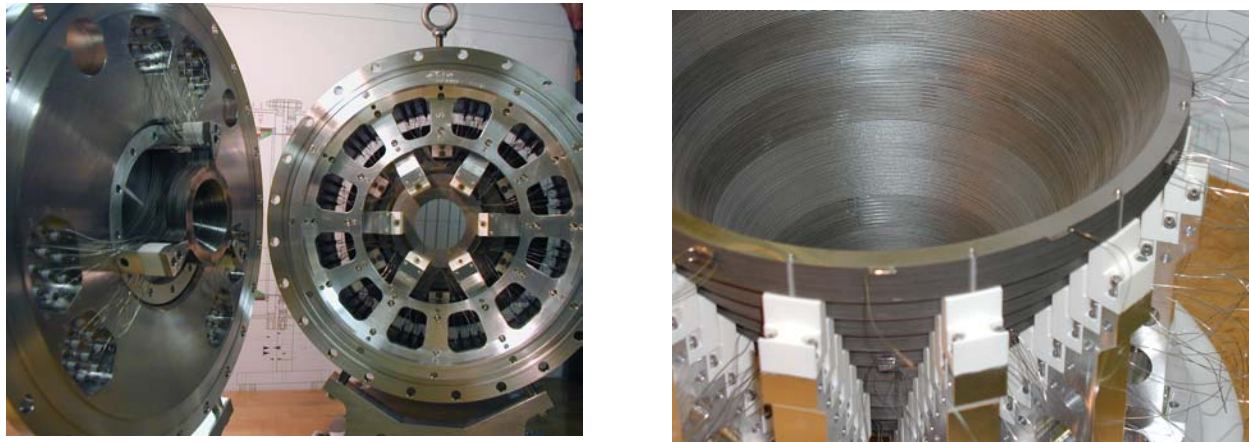[‡]GSI, D-64291 Darmstadt, Germany

Figure III-31. View of the 2 completed sections of the conical extraction region with its 277 electrodes providing both DC gradient and a strong RF field close to the cone that repels the recoil ions.

Figure III-32. View of the capacitors and resistors connected to the internal electrodes to feed the DC and RF fields and that form part of the tank tuned circuits.

The large catcher volume results in longer extraction paths compared to the CPT gas catcher, placing even tighter requirements on the purity of the buffer gas. The much increased surface area puts severe constraints on the outgassing rate from the surfaces. The components of the gas catcher were cleaned to UHV standards and the entire cell is comprised of bakeable metal and ceramic. The fully instrumented large gas catcher was

moved to the area II experimental area at ATLAS (see Figure III-33) for initial tests. The cell was first tested offline with a 5μCi [252]Cf fission source and degraders mounted inside the chamber in October 2002. The device was initially debugged and tested with activity from this source.
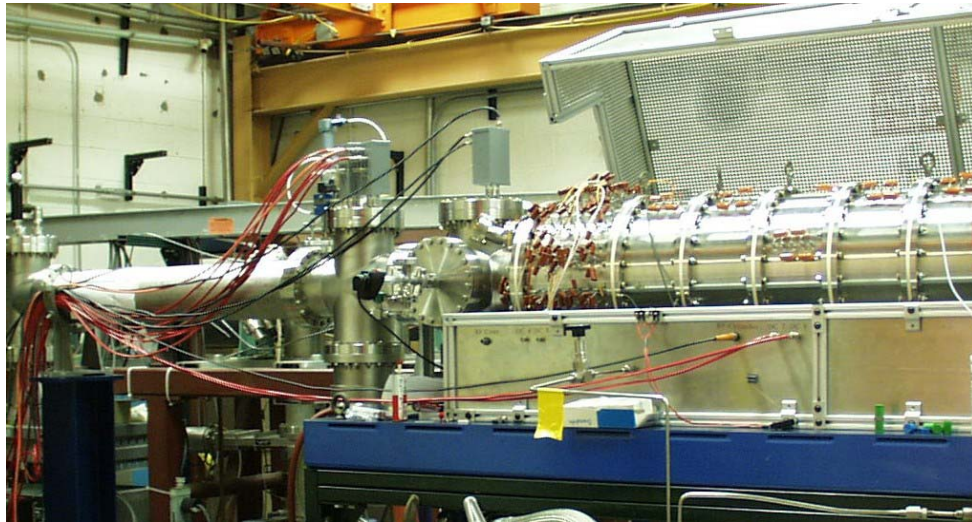

Figure III-33. RIA gas catcher prototype installed in the experimental area II at ATLAS. On the right we see the gas catcher inside the Faraday cage with the extraction section leading to the sections of RFQ. On the right we have the drift time-of-flight section leading to the detector system.

The gas catcher was then moved from target Area II and installed in the ATLAS general-purpose beamline. The catcher was attached to the ATLAS beamline by a ceramic insulator to allow high-voltage biasing of the cylinder itself and its vacuum separated from the beamline vacuum by an all-metal large-area 77cm^2 reinforced Havar window. In December 2002, the first on-line test of the full-scale prototype cell was performed by stopping and extracting a radioactive [25]Al beam provided by ATLAS through in-flight collection and separation of reaction products from a [2]H ([24]Mg, [25]Al) reaction on a cooled deuterium gas target. The collection efficiency of the catcher was measured as a function of the pressure and applied electric fields. The big catcher showed roughly 25% extraction efficiency for [25]Al at the maximum fields reached in this first test.

The on-line testing will continue in 2003 with numerous improvements including further development of the detection system to improve the mass identification of the extracted activity and better control of the radioactive beams injected from the ATLAS accelerator into the gas catcher. Off-line tests of the gas cell with a [252]Cf fission source between on-line tests will also continue, as are tests of the mass distributions of the extracted fission fragment species under different configurations of applied electric field and degraders. Since the gas pressure and the electric field determine the mean extraction time, the losses in the cell due to interactions with contaminants in the gas can be investigated. The performance of the catcher cell is limited by the strength of the achievable electric fields in the gas and by the accumulation of charge in the volume of the cell; efforts to quantify both of these limitations are underway. After completing testing at

ATLAS energies, the prototype will be moved to GSI's FRS where beam time has been approved for tests of the cell's performance at full RIA fragment energies.

_____
[1]G Savard et al, "Development and operation of gas catchers to thermalize fusion-evaporation and fragmentation products," NIM A 492 (2002) 57

c.5.   Assessment of E-Beam as a Monitoring Tool for Lithium Film Thickness
(Itacil Gomes and J. A. Nolen)

Calculations were performed to asses the potential application of a low energy (20-50 KeV) electron beam as a diagnostic tool to monitoring thin lithium film used as electron strippers for heavy-ion accelerators. The distribution of the electron scattered by the lithium is a function of the thickness of the lithium film. In this concept the low energy electron beam will not interfere with the interactions between heavy ions and lithium film and will have a negligible effect in the energy deposition in the lithium. The e-beam will be directed at an angle to the heavy ion beam and a collecting plate will be placed perpendicular to the e-beam direction at a distance that does not interfere with other accelerator structures (in the calculations a 30-cm distance was assumed).

Calculations were performed for lithium film thicknesses of 9, 10, 11, and 12 μm and electron beam energies of 20, 30, 40, and 50 KeV. It was observed that the lowest electron beam energy analyzed (20 KeV) was the one to provide the highest potential for discriminating the variation of thickness of the lithium film. Figure III-34 shows a plot of the fraction of electrons collected in a plate placed at 30 cm from the lithium film as a function of the radius of the plate. As can be noticed for a plate with 30 cm of radius the fraction of electrons collected in the plate varies from 52.1% for the 12-μm thick film to 68.4% for the 9-μm thick lithium film. There are larger percentage changes in charge fraction collected for the smaller diameter plates. These differences allow us to infer that a simple circuit to measure the charge of electrons collected by a plate would have enough discrimination potential to be a valuable on-line real-time diagnostic tool for the thickness of the lithium film.   This work should continue to include different e-beam energies and lithium film thicknesses.
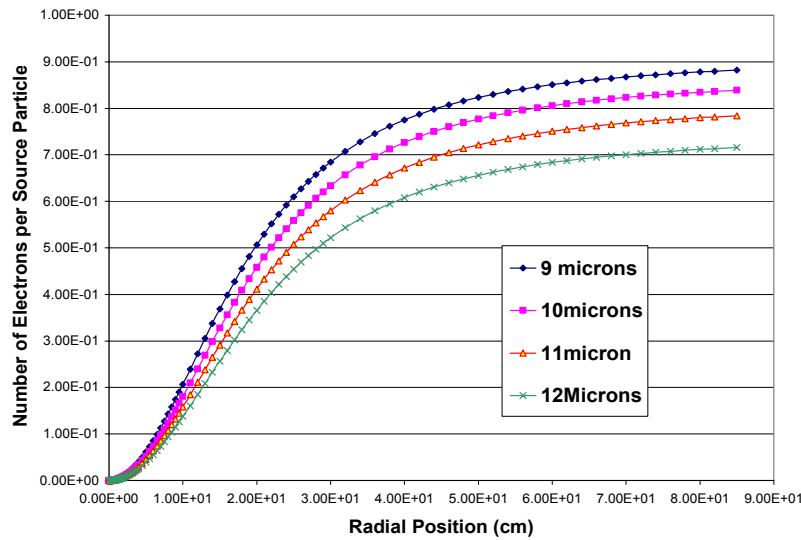

Figure III-34. Fraction of electrons collected in a plate placed at 30-cm from the lithium film as a function of the plate radius for a 20-KeV electron beam impinging on a thin-film of flowing lithium.

c.6.   Calculations of the Heat Deposition Profiles in a Lithium Jet by Electron Beams
(Itacil C. Gomes and J. A. Nolen)

The MCNPX[1] Monte Carlo transport code was used to simulate the interaction of electron beams with the lithium jet. The energy deposition profile inside the jet was scored in small volumes and input in the graphic program Origin[2] for displaying the information. The assumed lithium jet thickness was 1 cm and the e-beam energies 1, 3, and 5 MeV. The geometry was divided in 3300 meshes with 0.1 mm increments in the radial direction and 0.3 mm increments in the axial direction. The objective of the calculations was to verify if a uniform energy deposition profile across the lithium jet could be achieved to simulate the uranium beam energy deposition (in a fragmentation target of RIA) as it crosses the lithium jet.

Figures III-35, III-36, and III-37 display the energy deposition (MeV/cm^3-beam particle) in the lithium jet for the1, 3 and 5-MeV electron beam cases, respectively.   Figure III-35 shows that the 1-MeV electron beam loses most of its energy at half-way inside the target (at roughly 5mm) where the energy deposition is already reduced by more than one order of magnitude. The maximum energy deposition is about 103 MeV/cm^3 at positions close to the entrance of the beam into the jet. The calculated total energy deposited into the jet per incident electron is 0.997MeV, meaning that basically all energy carried by the beam is deposited into the jet. Figure III-36 shows that the 3-MeV electron beam is not "stopped" inside the lithium jet and it is still depositing 5-MeV/cm^3 at the beam center line after 1-cm of lithium. The maximum energy deposition is about 95 MeV/cm^3 at positions close to the entrance of the beam into the jet. The calculated total energy deposited into the jet per incident electron is 0.823 MeV, meaning that 17.7% of the energy carried by the beam is deposited elsewhere. This represents that for a 40 kW electron beam, about 33 kW will be deposited into the lithium.
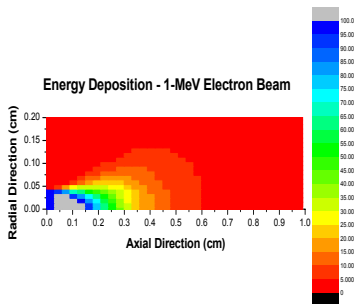

Figure III-35. Energy deposition profile in MeV/cm^3 along the thickness of the beam for a 1MeV electron beam incident on a fast-flowing lithium jet.
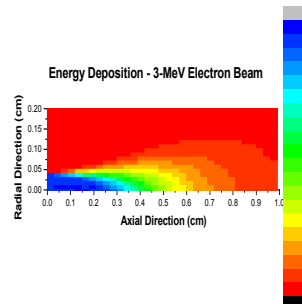
Figure III-36. Energy deposition (MeV/cm^3) profile for a 3-MeV electron beam incident on a fast-flowing lithium jet.
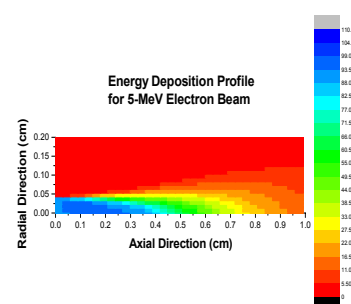
Figure III-37. Energy deposition (MeV/cm^3) profile for a 5-MeV electron beam incident on a fast-flowing lithium jet.

Figure III-37 shows that the 5-MeV electron beam is not "stopped" inside the lithium jet; it is still depositing 14-MeV/cm^3 in the center line of the beam after 1-cm of lithium. The maximum energy deposition is about 96 MeV/cm^3 at positions close to the entrance of the beam into the jet. The calculated total energy deposited into the jet per incident electron is 0.804 MeV, meaning that for a 40 kW electron beam, about 32 kW will be deposited into the jet. The maximum energy deposition of about 100 MeV/cm^3 is similar to that expected for a uranium beam hitting the lithium jet in the fragmentation target design.

Conclusions

The calculations indicated that there is no real gain in increasing the energy of the beam; the amount of energy deposited remains about the same. The energy deposition of the 1-MeV electron beam is much more concentrated in the first millimeters than in the other cases. The amount of energy escaping from the lithium jet is much larger in the high energy cases. The 1-MeV electron beam may present the best approach to simulate the energy deposition, due to its compactness in terms of energy deposition profile and the advantage of having the beam stopped inside the lithium jet. Also, the 1-MeV electron beam presents the highest overall energy deposition. The 3- and 5-MeV cases have a more concentrated energy deposition in the direction of the beam, and less scattering.

---

[1]Laurie Waters, editor, "MCNPX User's Manual – Version 2.3.0", April 2002, LA-UR-02-2607.
[2]Origin – Microcal Software Inc. One Roundhouse Plaza, Northhampton, MA 01060 USA